

Radiative forcing of anthropogenic aerosols on cirrus clouds using a hybrid ice nucleation scheme

Jialei Zhu^{1,2} and Joyce E. Penner²

1 Institute of Surface-Earth System Science, School of Earth System Science,
Tianjin University, Tianjin 300072, China

2 Department of Climate and Space Sciences and Engineering, University of
Michigan, Ann Arbor, Michigan 48109, USA

Corresponding Author: Jialei Zhu (Email: zhujialei@tju.edu.cn)

Abstract

Anthropogenic aerosols impact cirrus clouds through ice nucleation, thereby changing the Earth's radiation budget. However, the magnitude and sign of anthropogenic forcing in cirrus clouds is still very uncertain depending on the treatments for ice nucleating particles (INPs), for haze particle freezing, and the ice nucleation scheme. In this study, a new ice nucleation scheme (hereafter the HYBRID scheme) is developed to combine the best features of two previous ice nucleation schemes, so that global models are able to calculate the ice number concentration in both updrafts and downdrafts associated with gravity waves and has a robust sensitivity to the change of aerosol number. The scheme is applied in a box model, and the ice number concentrations ($9.52 \pm 2.08 \text{ L}^{-1}$) are somewhat overestimated but are in reasonable agreement with those from an adiabatic parcel model ($9.40 \pm 2.31 \text{ L}^{-1}$). Then, the forcing and cloud changes associated with changes in aircraft soot, sulfur emission and all anthropogenic emissions between the preindustrial (PI) period and the present day (PD) are examined using the

25 CESM/IMPACT global model with the HYBRID scheme. Aircraft soot emissions
26 decrease the global average ice number concentration (Ni) by $-1.0 \pm 2.4 \times 10^7 \text{ m}^{-2}$ (-
27 1%) (over the entire column) due to the inhibition of homogeneous nucleation and
28 lead to a radiative forcing of $-0.14 \pm 0.07 \text{ W m}^{-2}$, while the increase in sulfur emissions
29 increases the global average Ni by $7.3 \pm 2.9 \times 10^7 \text{ m}^{-2}$ (5%) due to the increase in
30 homogeneous nucleation and leads to a radiative forcing of $-0.02 \pm 0.06 \text{ W m}^{-2}$. The
31 possible effects of aerosol and cloud feedbacks to the meteorological state in remote
32 regions partly contribute to reduce the forcing and the change in Ni due to
33 anthropogenic emissions. The radiative forcing due to all increased anthropogenic
34 emissions from PI to PD is estimated to be $-0.20 \pm 0.05 \text{ W m}^{-2}$. If newly formed
35 secondary organic aerosols (SOA) act as INPs and inhibit homogeneous nucleation,
36 the Ni formed from heterogeneous nucleation is increased. As a result, the inclusion
37 of INPs from SOA increases the change in Ni to $12.0 \pm 2.3 \times 10^7 \text{ m}^{-2}$ (9%) and
38 increases (makes less negative) the anthropogenic forcing on cirrus clouds to -
39 $0.04 \pm 0.08 \text{ W m}^{-2}$ from PI to PD.

40

41 **1. Introduction**

42 Atmospheric aerosol loading has increased significantly since the PI period,
43 mainly due to anthropogenic emissions associated with the burning of fossil fuels
44 and biomass. Most studies to date have focused on how the increase in anthropogenic
45 aerosols impacts climate via warm clouds thereby exerting a net cooling effect
46 (Wang and Penner, 2009; Zhu et al., 2019; Gordon et al., 2016; IPCC, 2013).
47 Compared to warm clouds, there has been much less attention paid to anthropogenic
48 forcing as a result of changes to cirrus clouds, which is one of the least understood
49 processes in the climate system (Fan et al., 2016). Cirrus clouds cover about 30% of
50 the Earth's area (Wang et al., 1996) and play an important role in the Earth's

51 radiation budget and also influence global precipitation and the hydrologic cycle
52 (Waliser et al., 2009; Hong et al., 2016; Matus, A. V. and L'Ecuyer 2017). Ice
53 particles in cirrus clouds are nucleated on aerosol particles, so that changes to the
54 aerosol composition and loading may alter cirrus clouds by altering cloud
55 microphysics, resulting in a cirrus cloud radiative forcing.

56 There are major uncertainties in calculating the radiative forcing of cirrus clouds
57 using global climate models, both in terms of its magnitude (since PI) and its sign
58 (Storelvmo, 2017). The ice particles in the cirrus clouds can form either by
59 homogeneous freezing of solution droplets (or haze particles) (Koop et al., 2000) or
60 by heterogeneous nucleation of INPs (Cantrell and Heymsfield, 2005). Supercooled
61 aqueous solutions such as sulfate haze particles can form ice through homogeneous
62 nucleation when the relative humidity with respect to ice (RH_i) is high (of order
63 150%), which may be the dominant mechanism for the ice formation in cirrus clouds
64 (Hendricks et al., 2011; Kuebbeler et al., 2014; Penner et al., 2018). However,
65 heterogeneous ice nucleation of INPs formed from dust, soot and other insoluble
66 aerosols requires much lower RH_i, so that heterogeneous nucleation is able to occur
67 in advance of homogeneous nucleation in a rising air parcel (Hoose and Möhler,
68 2012). As a result, heterogeneous and homogeneous ice formation compete for the
69 available water vapor. Heterogeneous nucleation can lead to a significant reduction
70 of the number of ice particles that form compared to homogeneous freezing because
71 the number of INPs is much smaller than the number of haze particles. However, if
72 additional INPs are added to a region where heterogeneous nucleation already
73 dominates, an increase in ice crystal number is expected. Therefore, the radiative
74 effect of aerosols on cirrus clouds could differ in both magnitude and sign depending
75 on the competition between these two ice nucleation processes. Ice nucleation by

76 INPs vs haze freezing is determined by both the number of homogeneous and
77 heterogeneous ice nucleating particles as well as the updraft velocity or cooling rate.

78 Despite the relatively low level of understanding of ice nucleation, a few
79 physically based parameterizations that treat the competition between homogeneous
80 and heterogeneous nucleation have been developed in order to study the effect of ice
81 nucleation in global climate models (Liu and Penner, 2005; Kärcher et al., 2006;
82 Barahona and Nenes, 2008). The Liu and Penner (2005) parameterization (hereafter
83 LP) is derived from fitting the simulation results of an adiabatically rising cloud
84 parcel (Liu and Penner, 2005). The LP parameterization is only able to treat cases
85 for which the updraft velocity is positive, so the evaporation of drops during
86 downdrafts is neglected. The parameterization developed by Barahona and Nenes
87 (2008) (hereafter BN) is derived from an analytical solution of the cloud parcel
88 equations (Barahona and Nenes, 2008). The LP and BN parameterizations always
89 show a similar trend when there is an increase in either the haze aerosol number
90 concentrations or INPs, (Shi and Liu, 2018) and they result in very similar ice
91 number concentrations when the water vapor accommodation coefficient is set to
92 0.1 (Zhou et al., 2016). The Kärcher et al. (2006) parameterization (hereafter KL)
93 explicitly calculates the evolution of ice supersaturation in a rising cloud parcel when
94 different aerosol types freeze (Kärcher et al., 2006). The KL parameterization was
95 used in previous studies of the effect of aerosol particles on cirrus clouds because it
96 includes an explicit representation of the relevant physics (Penner et al., 2009;
97 Penner et al., 2018) and Penner et al. (2018) added the capability to represent
98 evaporation of water in downdrafts. However, in the KL parameterization, aerosol
99 particles in different size bins will freeze chronologically from the largest size bin
100 until the rate at which R_{Hi} decreases by water vapor deposition equals the rate at
101 which R_{Hi} increases as a result of temperature decreases. Under this assumption,

102 competition among different aerosol size bins for water deposition is not allowed.
103 As a result, the homogeneous freezing of some particles in small size bins is
104 underestimated in KL parametrization (Liu and Shi, 2018). The KL parametrization
105 results in a smaller sensitivity to increases in sulfate aerosol number than the LP and
106 BN parametrizations except at very low sulfate number concentrations, while the
107 three parameterizations have similar sensitivity to the number concentration of INPs
108 (Shi and Liu, 2018).

109 Global numerical simulation experiments of aerosol effects on cirrus cloud
110 formation have been carried out in a limited number of studies with different ice
111 nucleation parameterizations and updraft treatments. Penner et al. (2009) used the
112 KL and LP parameterizations to estimate the radiative forcing of aerosols on cirrus
113 clouds using an off-line ice nucleation and radiative transfer model. They found a
114 negligible forcing from sulfate but a significant cooling (ranging from -0.38 to -0.56
115 W m^{-2}) from surface-based and aircraft emissions of soot with the assumption that
116 100% of soot particles are efficient INPs (Penner et al., 2009). As a result, the
117 radiative forcing of all anthropogenic aerosols was estimated to be -0.53 to -0.67 W
118 m^{-2} using the LP and KL parameterizations. However, observations later indicated
119 that only 0.01 to 0.1% of the less-hygroscopic soot from fossil fuels and biomass
120 fires act as good INPs at supersaturations near 140% RH_i and low temperatures
121 (Koehler et al., 2009; Pratt et al., 2011; Prenni et al., 2012). Gettelman et al. (2012)
122 used the LP and BN parameterizations and calculated that the radiative forcing
123 associated with aerosol effects on cirrus clouds is $0.27 \pm 0.10 \text{ W m}^{-2}$ (the uncertainty
124 is the standard deviation of the interannual variations hereafter) as a consequence of
125 increasing anthropogenic sulfur emissions (with no effect from soot) (Gettelman et
126 al., 2012).

127 In addition to assumptions of the extent to which soot might act as an INP, a
128 second source of uncertainty in the calculation of aerosol forcing in cirrus clouds is
129 the treatment of the sub-grid scale updraft velocity used in the nucleation scheme
130 (Zhou et al., 2016). Penner et al. (2009) used a normal probability distribution with
131 a standard deviation of 0.33 m s^{-1} (Penner et al., 2009) while Wang and Penner (2010)
132 used a single updraft velocity based on the standard deviation of mesoscale
133 temperature fluctuations associated with gravity waves (Wang and Penner, 2010).
134 Other models chose a sub-grid scale updraft velocity associated with the predicted
135 turbulent kinetic energy (Liu et al., 2012; Kärcher and Lohmann, 2002; Lohmann,
136 2002; Lohmann et al., 1999). Joos et al. (2008) added the effect of the contribution
137 of orographic waves to the vertical velocity. Penner et al. (2018) first used a wave
138 spectrum (instead of a constant updraft velocity) together with the KL
139 parameterization to treat the formation of ice crystals. They used the equatorial
140 spectrum of observed gravity waves presented by Podglajen et al. (2016) together
141 with the seasonal and latitudinal variations determined by Gary (2006) and Gary
142 (2008). They also varied the standard deviation from Podglajen et al. (2016) based
143 on the vertical stratification of atmospheric stability, the atmospheric density and
144 topography. However, the radiative forcing of sulfate as well as all anthropogenic
145 aerosols were not explored due to the deficiencies in the KL parameterization (Liu
146 and Shi, 2018).

147 Secondary organic aerosols (SOA) have been shown to have a highly viscous
148 semisolid or even glassy state at low temperatures and low RH_i in many experiments
149 (Koop et al., 2011; Pajunoja et al., 2014; Renbaum-Wolff et al., 2013; Saukko et al.,
150 2012). Observations also found SOA acting as IN and in the ice crystal residues of
151 cirrus clouds (Ignatius et al., 2016; Wagner et al., 2017; DeMott et al., 2003; Cziczo
152 et al., 2013; Wilson et al., 2012). A peak in the number concentration of ultrafine

153 particles were observed near 12km in the Amazon and identified as primarily organic.
154 Furthermore, a marker molecule indicated that a substantial fraction of the organics
155 in aerosol-rich layers in the upper troposphere were associated with the oxidation of
156 isoprene (Andreae et al., 2018). A modelling study that included the nucleation of
157 new particles through organic nucleation predicted that there are a large number of
158 accumulation mode SOA particles existing in the upper tropical troposphere which
159 may be important for the ice nucleation (Zhu and Penner, 2019). SOA particles have
160 a strong potential to act as INPs to form ice particles via heterogeneous freezing
161 under the conditions conducive to ice formation in the upper troposphere (Knopf et
162 al., 2018). However, the influence of SOA on cirrus clouds is not yet fully studied
163 (but see Penner et al., 2018).

164 In this study, we combined the best features of the LP and KL parameterizations
165 to develop a hybrid ice nucleation scheme that accounts for the changes in ice
166 number concentrations in both the updrafts and downdrafts associated with a
167 spectrum of gravity waves. Using a global climate model coupled with the new ice
168 nucleation scheme, the radiative forcing of aircraft soot and sulfate were examined.
169 Furthermore, the radiative forcing of anthropogenic aerosols on cirrus clouds since
170 the PI time period was estimated both including and excluding the effect of changes
171 in SOA. A global average negative anthropogenic forcing of $-0.20 \pm 0.05 \text{ W m}^{-2}$
172 without SOA as a result of aerosol effects in cirrus clouds is suggested. The forcing
173 is reduced to $-0.04 \pm 0.08 \text{ W m}^{-2}$ when SOA is included.

174

175 **2. Methodology**

176 **2.1 Model**

177 We used the Community Earth System model (CESM) version 1.2.2 (refer to
178 <http://www.cesm.ucar.edu/models/cesm1.2/> for details) coupled to the University of
179 Michigan IMPACT aerosol model (Liu et al., 2005 with updates as described herein)
180 with a resolution of 1.9° (longitude) \times 2.5° (latitude) and 30 vertical layers to simulate
181 aerosols and their effects on cirrus clouds. This version of the IMPACT model
182 simulates the number and mass of pure sulfate in three modes (i.e. nucleation (<5
183 nm), Aitken (5-50 nm) and accumulation (>50 nm)) and their interaction with the
184 following fourteen other aerosol species/types. Sulfate is the only aerosol
185 participating in homogeneous ice nucleation in the model. Soot from fossil fuel and
186 biofuel burning (fSoot) is simulated in three modes with different hygroscopicity
187 according to the number of monolayers sulfate on its surface (Yun et al., 2013) while
188 soot from biomass burning (bSoot) is simulated in one mode. 0.05% of fSoot with
189 <1 monolayers of sulfate and 0.1% of fSoot coated with 1-3 monolayers of sulfate
190 as well as 0.1% of bSoot are assumed to be effective INPs. The hygroscopicity of
191 fSoot and bSoot is determined by volume averaging the hygroscopicity of the
192 underlying particles and the number of sulfate monolayers on the particles. Aircraft
193 soot is simulated in two modes. The first mode has acted as an ice nuclei within
194 contrails that subsequently evaporated (cSoot). The 2nd mode which has not been an
195 ice nuclei within contrails is not considered to act as an INP in the model. The soot
196 that has already been included in contrail ice is pre-activated. We assume the pre-
197 activated aircraft soot coated with less than 3 monolayers of sulfate to be an INP
198 similar to the treatment in Zhou and Penner (2014) (see also Mahrt et al., 2019). Dust
199 and sea salt are each carried in four separate bins with varying radii. Dust with fewer
200 than 3 monolayers of sulfate coating is used to form heterogeneous INP in the model.

201 This treatment is consistent with the results of field studies by DeMott et al. (2003),
202 Cziczo et al. (2004) and Richardson et al. (2007). The assumptions for aerosols to
203 be effective INPs in the model are summarized in Table 1. The aerosols simulated
204 by the IMPACT model are only able to nucleate the initial ice crystal number
205 concentration in cirrus clouds in the CESM model. Thereafter, the growth and
206 sedimentation as well as evaporation of ice crystals follow the treatment in the
207 CESM. In addition, the changes to cirrus clouds have feedbacks as a result of
208 changes to the radiation budget, temperature, and the formation of warm clouds, as
209 simulated in the CESM model.

210

211 2.2 Ice nucleation parameterization

212 The LP parameterization is only able to calculate the ice nucleation in a rising
213 parcel, but is not able to predict the changes in the supersaturation or simulate the
214 evaporation of ice in downdrafts. As a result, the scheme used by Penner et al. (2018)
215 to treat gravity waves cannot be used with the LP parameterization as it was
216 originally formulated. The KL scheme calculates the changes in the sub-grid scale
217 variation of RH_i in a cloud parcel as a result of updrafts or downdrafts and the growth
218 or decay of ice particles. Unlike some schemes (e.g. Shi et al., 2015) which consider
219 that the initial nucleation in an updraft takes place in the presence of ice from the
220 previous time step, we assume the first parcel updraft within a GCM time step does
221 not carry any preexisting ice, but thereafter if ice forms it may either grow and
222 decrease the supersaturation or evaporate adding water vapor to the parcel. However,
223 aerosols freeze in the order of size bins and this neglects the competition among
224 different aerosol size bins, which results in an underestimation of the ice formed
225 from aerosols in small size bins and a low sensitivity to the change of aerosol number

226 (Liu and Shi, 2018). In this study, we combined the LP and KL parameterizations to
 227 develop a new ice nucleation scheme (hereafter HYBRID) to make use of their
 228 strengths and avoid their defects.

229 In the HYBRID scheme, the supersaturation (S_i) in the cloud parcel is
 230 calculated explicitly using the KL scheme so that ice particles are able to grow or
 231 decay throughout the time variations in the updrafts and downdrafts associated with
 232 gravity waves. S_i is calculated as a function of the updraft and aerosol concentrations
 233 at each grid. S_i is updated every second using

$$234 \quad \frac{dS_i}{dt} = a_1 S_i w - (a_2 + a_3 S_i) \int_0^\infty dr_0 \frac{dn}{dr_0} R_{im}(r_0)$$

235 where the parameter a_1 is given by $a_1 = (L_s M_w g)/(c_p R T^2) - M g/(R T)$, with the
 236 molar mass of air M and water M_w , latent heat of sublimation L_s , constant of gravity
 237 g , heat capacity at constant pressure c_p , the universal gas constant R , and air
 238 temperature T . w is the vertical velocity. $a_2 = 1/n_{sat}$ with the water vapor number
 239 density at ice saturation n_{sat} . $a_3 = L_s^2 M_w m_w/(c_p p T M)$, with the mass of a water
 240 molecule m_w and the air pressure p . R_{im} is the monodisperse freezing/growth integral,

$$241 \quad R_{im} = \frac{4\pi}{v} \int_{-\infty}^t dt_0 \dot{n}_i(t_0) r_i^2(t_0, t) \frac{dr_i}{dt}(t_0, t),$$

242 where v is the specific volume of a water molecule. $dt_0 \dot{n}_i(t_0)$ is the number density
 243 of aerosol particles that nucleate ice and freeze within the time interval between t_0
 244 and $t_0 + dt_0$, $r_i(t_0, t)$ is the radius of the spherical ice particle at time t that froze
 245 and commenced to grow at time $t < t_0$, and dr_i/dt is the radial growth rate of that
 246 ice particle. In the HYBRID scheme, $\dot{n}_i(t_0)$ is determined using the LP
 247 parameterization.

248 A series of updraft velocities at each grid point was generated based on a fitted
 249 wave spectrum to the observed equatorial gravity waves from Podglajen et al. (2016).
 250 The standard deviation of this wave spectrum was extended to other latitudes and

251 seasons by using the parameterization proposed by Gary (2006, 2008). It was
 252 extended vertically based on the static stability, atmospheric density and topography.
 253 This parameterization of the wave spectrum associated with gravity waves is
 254 described in Penner et al. (2018).

255 When the updraft velocity is positive, the LP parameterization is used to
 256 calculate the increase in the ice number from homogeneous and/or heterogeneous
 257 freezing, so that the HYBRID scheme avoids the lack of sensitivity to changes in
 258 aerosol number in the KL parameterization when calculating the number of new ice
 259 particles. The LP parameterization is derived by fitting the results of a large set of
 260 parcel model simulations covering different conditions in the upper troposphere (Liu
 261 and Penner, 2005). Two separate regimes are identified by the sign of $T -$
 262 $6.07 \ln w + 55.0$ (where T is the temperature and w is the updraft velocity) to
 263 calculate the change of N_i due to homogeneous nucleation. When the sign is positive,
 264 the solution is in fast-growth regime which is associated with higher T and lower w .
 265 The number concentration of new ice crystals (N_i or $\dot{n}_i(t_0)$ as in the above) is then
 266 calculated with the following equation

$$267 \quad N_i = \min\{\exp(a_2)N_a^{a_1}\exp(bT)w^c, N_a\}$$

268 where $b = b_1 \ln N_a + b_2$, and $c = c_1 \ln N_a + c_2$. N_a is the number concentration of
 269 sulfate in the Aiken and accumulation modes. The coefficients $a_1, a_2, b_1, b_2, b_3, c_1,$
 270 c_2 are constant, and can be found in Table 1 of Liu and Penner (2005). For lower T
 271 and higher w (the slow-growth regime), the following equation is applied to calculate
 272 N_i :

$$273 \quad N_i = \min\{\exp[a_2 + (b_2 + b_3 \ln w)T + c_2 \ln w]N_a^{a_1 + b_1 T + c_1 \ln w}, N_a\}$$

274 where the coefficients $a_1, a_2, a_3, b_1, b_2, b_3, c_1, c_2$ are again listed in Table 1 of Liu
 275 and Penner (2005) and are different from those in the fast-growth regime. The

276 number concentration of N_i from INPs in the heterogeneous nucleation regime is
 277 given as

$$278 \quad N_i = \min\{exp(a_{22})N_{INP}^{b_{22}}exp(bT)w^c, N_{INP}\}$$

279 where $b = (a_{11} + b_{11} \ln N_{INP}) \ln w + (a_{12} + b_{12} \ln N_{INP})$ and $c = a_{21} + b_{21} \ln N_{INP}$.
 280 N_{INP} is the number concentration of total INPs. The coefficients a_{11} , a_{12} , a_{21} , a_{22} , b_{11} ,
 281 b_{12} , b_{21} , b_{22} can be found in the Section 4.2 of Liu and Penner (2005). When the
 282 updraft velocity is low and temperature is high, heterogeneous ice nucleation takes
 283 place initially and depletes the water vapor in the parcel so that homogeneous ice
 284 freezing never occurs. The threshold temperature T_c for heterogeneous nucleation-
 285 only is given by

$$286 \quad T_c > a \ln(w) + b$$

287 where $a = -1.4938 \ln(N_{INP}) + 12.884$; $b = -10.41 \ln(N_{INP}) - 67.69$. When the
 288 regime is in a transition from heterogeneous-dominated to the homogeneous-
 289 dominated regimes, the total ice number concentration from nucleation can be higher
 290 than the ice concentration from only heterogeneous nucleation, but lower than that
 291 from the pure homogeneous nucleation case. Then, N_i is interpolated from

$$292 \quad N_i = N_{Het} \left(\frac{N_{Het}}{N_{Hom}} \right)^{\frac{N_{INP} - N_c}{0.9 N_c}}$$

293 where N_{Het} is the ice number from pure heterogeneous nucleation, N_{Hom} is the ice
 294 number from pure homogeneous nucleation, N_{INP} is the number concentration of
 295 INPs and N_c is the critical number concentration of INPs for the heterogeneous
 296 nucleation-only regime.

297 Based on the method outlined above, HYBRID scheme calculates the increase
 298 in N_i using LP parameterization. The new ice crystals from nucleation either grow
 299 or decay with consumption/evaporation of water vapor and therefore change S_i ,

300 which is determined using KL parameterization. The changes in S_i then influence
301 which particles are able to nucleate forming ice crystals.

302 We define cirrus clouds for which the effects of aerosols are defined/calculated
303 as all large-scale clouds formed at temperatures $< -35^\circ\text{C}$. Cirrus clouds at these
304 temperatures include anvil cirrus that are formed by the outflow from deep
305 convection as well as large-scale cirrus formed by in-situ gravity waves. The
306 detrained ice crystal number concentration in anvils is calculated from the detrained
307 ice mass by assuming a spherical particle with a constant volume-mean radius,
308 which is approximated as $3\rho_0 Q / (4\pi\rho_i r_{iv}^3)$ following Lohmann (2002). ρ_i is the ice
309 crystal density, ρ_0 is the air density, r_{iv} is the volume mean radius determined from
310 a temperature-dependent lookup table (Kristjánsson et al. 2000; Boville et al. 2006),
311 Q is the detrainment rate of cloud water mass diagnosed from the convection
312 parameterization. The new clouds generated by convective detrainment are assumed
313 to be at saturation with respect to ice. In doing this, anvil clouds and in situ cirrus
314 compete for the available water vapor within a grid box. When anvil clouds are
315 formed due to convective detrainment, it reduces the saturation ratio in the clear-sky
316 portion of a grid, and can potentially reduce the frequency of in situ large-scale cirrus
317 formation (Wang and Penner 2010; Wang et al. 2014). We only calculate N_i as a
318 result of the nucleation of aerosol in large-scale cirrus, so that when anvils occur in
319 a grid box, we average the concentrations to determine the total ice number
320 concentration in cirrus clouds. Anthropogenic emissions contribute to the change in
321 the number concentration of ice crystals in large-scale cirrus cloud, but these are
322 then averaged with the crystals in anvils.

323

324 2.2.1 Evaluation of the HYBRID scheme

325 In order to examine the ability of the HYBRID ice nucleation scheme to
326 simulate ice number concentration, the results from a box model using the HYBRID

327 scheme are compared with those from an adiabatic parcel model under the same
328 simulation conditions. The adiabatic parcel model was that used to generate the LP
329 parameterization and was introduced in Liu and Penner (2005). The two models are
330 run for 30 min for each simulation, which is the time step used in the CESM. During
331 the 30 min, the updraft velocity is updated every 2.2 min as recommended by
332 Podglajen et al. (2016). The ice number concentrations after the 30 min simulation
333 from the two models are compared. We ran both the adiabatic parcel model and the
334 HYBRID box model using a constant updraft velocity for each 2.2-min interval.
335 When the velocity is positive ice crystals form and grow in the HYBRID box model
336 as described above. For downdrafts, if the supersaturation is below 100%, the two
337 models use the same method to simulate the evaporation of any existing ice particles,
338 which is also the same method used in the global model as suggested in Kärcher et
339 al. (2006). The scheme used here for the HYBRID box model is the same as the
340 HYBRID scheme used in the global model. Note that the final interval within each
341 30 minute simulation is shortened in order to match the treatment used in the
342 CESM/IMPACT model which uses a 30 minute time step. When run within the
343 CESM model, this final ice number concentration is then passed back to the CESM
344 model after this 30 minute interval.

345 The updrafts and downdrafts associated gravity waves are determined from a
346 Laplace distribution as suggested by the fit to the observed gravity waves by
347 Podglajen et al. (2016). We conducted 10,000 simulations using a random selection
348 of the updrafts and downdrafts for each model. Both models use the same selection
349 of updrafts and downdrafts in each simulation. We set up an initial condition with a
350 temperature of 230K, the standard deviation for the updraft velocities was 0.5 m s^{-1}
351 and the initial RH_i was 130%. The sulfate number concentration was set to 0.2 L^{-1}

352 while the dust concentration was 10 L^{-1} . These particles then participate in either
353 homogeneous nucleation or heterogeneous immersion nucleation.

354 Figure 1 shows a histogram of the predicted ice number concentration (N_i) for
355 10,000 simulations of the adiabatic parcel model and the box model using the
356 HYBRID scheme. Two populations of N_i are shown in Figure 1. The lower
357 population (with concentrations of the order of 10 L^{-1} or less) represents primarily
358 heterogeneous nucleation on dust particles, while the higher population (with
359 concentrations of the order of 10^2 L^{-1} or more) represents primarily homogeneous
360 nucleation on sulfate aerosols. The results in the simulations dominated by
361 heterogeneous nucleation are mostly similar for the two models, although the
362 HYBRID scheme overestimates the N_i between $1\sim 10 \text{ L}^{-1}$ when the results from the
363 adiabatic parcel model are less than 10^{-1} L^{-1} for some of these same simulations. The
364 average N_i from heterogeneous nucleation over 10,000 simulations from the
365 adiabatic parcel model is $9.40\pm 2.31 \text{ L}^{-1}$, while that from the HYBRID scheme is
366 $9.52\pm 2.08 \text{ L}^{-1}$.

367 The box model using the HYBRID scheme predicts larger N_i from
368 homogeneous nucleation than the parcel model in the 88% of simulations where
369 homogeneous nucleation occurs. There are more simulations using the HYBRID
370 scheme that predict larger N_i from homogeneous nucleation than the parcel model
371 as indicated by larger number of counts of large N_i (10^4 L^{-1} or more) in Figure 1.
372 The HYBRID scheme uses the LP parameterization for every small time step of 2.2
373 min. Since the LP parameterization was built using the largest N_i in an ascending
374 parcel after 30 min, there is a tendency for the HYBRID scheme to overpredict N_i .
375 The average N_i from homogeneous nucleation over the 10,000 simulations in the
376 two models is $1.41\pm 4.23 \text{ L}^{-1}$ from the parcel model, while it is $1.52\pm 4.83 \text{ L}^{-1}$ from
377 the HYBRID model. The HYBRID scheme overestimates the N_i from homogeneous

378 nucleation by 7.4%, which dominates the difference in total Ni between two models.
379 Overall, the average total Ni over the 10,000 simulations is $1.53 \pm 4.83 \text{ L}^{-1}$ using the
380 HYBRID scheme, which is 7.3% larger than the result from the parcel model
381 ($1.42 \pm 4.23 \text{ L}^{-1}$). We also examined the difference between the above case when
382 sulfate was 200 cm^{-3} compared to when sulfate was 20 cm^{-3} , and the difference was
383 within 7.2% of that using the full parcel model. Although the HYBRID scheme
384 predicts a somewhat larger number of nucleated ice particles, on average, the results
385 are reasonable compared to the results from the parcel model.

386

387

388 2.3 Experiments with the global model

389 We performed a series of model experiments in which different emissions of
390 aerosols and aerosol precursors are used. Table 2 provides a summary of these
391 experiments. The base case (PD_Base) uses emissions for the present day (PD, for
392 the year 2000) for anthropogenic sulfur and soot from fossil fuel adopted from
393 Community Emission Data System (CEDS) (Hoesly et al., 2018). Emissions from
394 van Marle et al. (2017) are adopted for biomass burning emissions. These emissions
395 are the same as the emissions datasets used for the CMIP6 simulations. The year
396 2000 emissions are used for all years of our simulation. We included soot from
397 aircraft for 2006 based on the Aviation Environment Design Tool (AEDT) data set
398 (Barrett et al., 2010). The AEDT data are presumed to be more accurate than the
399 CMIP6 aircraft emissions since they were developed based on the original flight
400 tracks of each of 31 million commercial flights worldwide (Wilkerson et al., 2010).
401 The dimethylsulfide (DMS) emissions from the ocean are assumed constant in the
402 PD and PI periods (Tilmes et al., 2016). The emission of dust uses the scheme from
403 Zender et al. (2003). In a sensitivity experiment (PI_cSoot), the emission of cSoot is

404 removed from PD_Base to examine its impact on ice number concentration and
405 radiative forcing. We also set a case (PI_SO4) with the emission of anthropogenic
406 sulfur changed to PI (≈ 1750) to calculate the radiative forcing of sulfur. The case
407 PI_ALL set all emissions to those of the PI period (≈ 1750) to examine the radiative
408 forcing of all anthropogenic aerosols on cirrus cloud. Additionally, we set up two
409 experiments to examine the effect of SOA as an INP on anthropogenic forcing in
410 cirrus clouds. The case PD_SOA and PI_SOA adds newly nucleated SOA particles
411 that have grown to the accumulation mode as additional INPs to the cases of
412 PD_Base and PI_ALL. The cases including SOA in the PD and PI read in the explicit
413 number concentration of newly formed SOA in the accumulation mode nucleated
414 from highly oxygenated organic molecules (HOMs) that form from the oxidation of
415 α -pinene. The nucleated SOA particles grow by deposition and coagulation of
416 sulfuric acid as well as the oxidation products of isoprene, α -pinene, limonene and
417 aromatics, that are in the aerosol phase. This SOA was simulated using the version
418 of the CESM/IMPACT model outlined in Zhu et al. (2017, 2019) and Zhu and
419 Penner (2019, 2020). The SOA that meets the requirements of the glass transition
420 temperature and RHi calculated using the equations in Wang et al. (2012) acts as an
421 effective heterogeneous INP.

422 The changes in aerosol emissions only influence the number concentration of
423 ice nuclei in the CESM, and thereby give the indirect radiative effect in cirrus clouds.
424 The direct radiative effect caused by the change of aerosols is not included. Clear
425 sky radiative forcing in this study is not associated with direct aerosol radiative
426 forcing, but is rather mainly due to changes in water vapor which leads to changes
427 in the clear sky longwave radiation (Wang and Penner, 2010). All cases were run
428 with prescribed sea surface temperatures for the present day and winds were nudged
429 towards ECMWF reanalysis data for the years 2005-2011 using a nudging time of 6

430 hours (Zhang et al., 2014). The data for the last six years were used for analysis in
431 this study.

432

433 **3. Results from the global model**

434 **3.1 Ice number concentrations**

435 The predicted N_i in PD_Base case is compared with the observed N_i reported
436 by Krämer et al. (2009) and Krämer et al. (2020) in Figure S1. Data from the model
437 have been selected to have ice water mixing ratios $> 10^{-8}$ kg kg⁻¹ to match values
438 seen in the in-situ observations (Krämer et al., 2016). The global model using the
439 HYBRID scheme is able to do a reasonable job in predicting N_i with the difference
440 in the median value between the simulation and observation less than 50% for all
441 temperatures except for the high concentrations seen between 197K and 213K. The
442 model predicts ~ 3 times higher N_i on average compared to the observations
443 between 197K and 213K. Although the comparison of ice number concentration
444 between our model and observation has not improved significantly compared to
445 that shown by Penner et al. (2018), the new nucleation scheme improves the ability
446 of nucleation to occur on small sized particles, since it avoids the calculation of ice
447 nucleation chronologically from large sizes to small size used in the KL scheme,
448 which results in an underestimation of ice crystals formed from small size particles.

449 The global average N_i in the PD_Base is 0.15×10^{10} m⁻² with the largest N_i in
450 the tropics of Eastern Hemisphere (Figure 2a). Most ice particles nucleate in the
451 upper troposphere (150~200 hPa) in the tropics, while some ice nucleation occurs
452 in the lower troposphere (around 300 hPa) in the polar regions (Figure 2b). The ice
453 particles formed from homogeneous nucleation dominate the total N_i in most
454 regions over the world (Figure S2a) and are responsible for $\sim 95\%$ of global average

455 Ni (Figure 2c). The large number concentration of sulfate in the Aitken and
456 accumulation modes in the upper troposphere over the west Pacific Ocean and
457 north Indian Ocean contributes to the remarkably large N_i in the tropical Eastern
458 Hemisphere. Heterogeneous nucleation dominates the N_i in the northern middle-
459 high latitudes where anthropogenic soot emission is high (Figure S2a), although
460 the N_i from heterogeneous nucleation is high in the tropics (Figure 2e).
461 Homogeneous nucleation mostly occurs in the upper troposphere (around 200hPa
462 in the tropics and around 300hPa in the extratropical regions), while heterogeneous
463 nucleation is an important contributor to N_i in the middle and lower troposphere
464 (Figure S2b). Although the N_i from homogeneous nucleation is high, the
465 occurrence frequency of homogeneous nucleation (calculated as the ratio of the
466 time steps when homogeneous nucleation occurs to all time steps with nucleation
467 occurring) is up to ~20% in the tropics and < 5% in most other regions (Figure S2c).
468 Due to the lack of the effect of orographic wave on ice nucleation, the observed
469 increases in ice number over orography, particularly over the Andes, Rockies, the
470 Antarctic mountains, and Greenland are not shown in Figure 2.

471 The competition between the heterogeneous INPs and homogeneous haze
472 particles determines the change in N_i between the PD and PI periods. We set up three
473 sensitivity cases to separately examine the effects of the emission of cSoot for
474 aircraft, anthropogenic sulfur and all anthropogenic emissions on N_i . INPs always
475 nucleate prior to homogeneous nucleation in a rising air parcel, so they consume the
476 available water vapor and inhibit homogeneous freezing when added to regions
477 dominated by homogeneous nucleation. The N_i formed from heterogeneous
478 nucleation increases significantly around 200hPa over the world due to the inclusion
479 of INPs from cSoot, especially near Southeast Asia (Figure 3e, 3f). Simultaneously,
480 homogeneous nucleation is inhibited significantly around 200hPa in Southeast Asia
481 and other tropical regions (Figure 3c, 3d). The emissions of aircraft soot that form

482 contrails peak near 200hPa with the spatial distribution shown in Figure 1a in the
483 Zhou and Penner (2014). Although the emissions of aircraft soot are large in
484 midlatitude, the effect of inhibiting homogeneous nucleation as a result of adding
485 the heterogeneous nucleation is large in the tropics (Figure 3c). That is because of
486 the largest number concentration of ice nuclei from homogeneous nucleation in the
487 tropics as shown in Figure 2c. Due to the much larger decrease in N_i from
488 homogeneous nucleation than the increase in N_i from heterogeneous nucleation, the
489 global average N_i is decreased by $0.1 \times 10^8 \text{ m}^{-2}$ (1%) when including the emission of
490 aircraft soot (Figure 3a). The change in N_i due to cSoot is small with a significant
491 change only over the North Atlantic Ocean and east coastal regions in North America
492 (Figure 3a).

493 In contrast to the case of aircraft soot, the increase in the sulfur emissions from
494 PI to PD leads to a large increase in N_i from homogeneous nucleation in most regions,
495 which causes an increase of $1.01 \times 10^8 \text{ m}^{-2}$ in the global average N_i (Figure 4c). The
496 increase in N_i from homogeneous nucleation contributes to the significant increase
497 in N_i near 150hPa over South Asia, Africa and the North Indian Ocean (Figure 4a).
498 The decrease in N_i from heterogeneous nucleation offsets some of the increase in N_i
499 from homogeneous nucleation and leads to a significant decrease in N_i near 300hPa
500 over the North Pacific Ocean (Figure 4a). In total, the global average N_i is increased
501 by $0.73 \times 10^8 \text{ m}^{-2}$ (5%) due to the increase in sulfur emissions.

502 The change in N_i from PI to PD due to all anthropogenic emissions is a balance
503 among the effects of increasing INPs from surface emissions and aircraft soot as
504 well as the increase in haze particles. The effect of all anthropogenic emissions on
505 N_i is mostly dominated by the increase in N_i from homogeneous nucleation caused
506 by the increase in sulfur emissions, but homogeneous nucleation is inhibited
507 somewhat by increased INPs from soot (compare Figure 5c and 4c). As a result, the

508 global average increase in *Ni* from homogeneous nucleation between PD_Base and
509 PI_ALL is only 58% of that between PD_Base and PI_SO4. The change in *Ni* from
510 heterogeneous nucleation is decreased in the mid-high latitudes of the Northern
511 Hemisphere (NH) from PD_Base to PI_ALL similar to the decrease from PD_Base
512 to PI_SO4 (Figure 5e, 5f). However, the increase in INPs from soot near Southeast
513 Asia leads to a small increase in *Ni* from heterogeneous nucleation there (Figure 5e).
514 In total, the increase in all anthropogenic emissions causes a significant increase of
515 *Ni* in South Asia and the North Indian Ocean while a significant decrease of *Ni* is
516 found in mid-latitude regions and some Arctic regions, resulting in $0.49 \times 10^8 \text{ m}^{-2}$ (3%)
517 more *Ni* from PI to PD for the global average.

518 It is conspicuous that sulfur and aircraft soot emissions have effects with different
519 signs for the change in *Ni* (Figure 3a, 4a). Generally, INPs from aircraft soot
520 decrease *Ni* due to the suppression of homogeneous nucleation in the regions
521 dominated by homogeneous nucleation, while the increase in sulfur emissions
522 increases *Ni* in these same regions due to the enhancement of homogeneous
523 nucleation. However, the changes to *Ni* have opposite signs in the west Pacific Ocean
524 off the coast of Southeast Asia, where the homogeneous nucleation is most active
525 (Figure 2c). We attribute this to the possible effect of aerosol and cloud feedbacks
526 to the meteorological state. When including aircraft soot, the temperature is
527 decreased (Figure S3b) and the RH_i is increased (Figure S3a) around 150hPa over
528 the west Pacific Ocean, where *Ni* from homogeneous nucleation increases a lot
529 (Figure 3c). The decrease in temperature is beneficial to homogeneous nucleation.
530 Meanwhile, the emission of aircraft soot is very low in the west Pacific Ocean due
531 to the lack of flight routes there (refer to Figure 1a in Zhou and Penner (2014)), so
532 that the effect of aircraft soot on the suppression of homogeneous nucleation is weak
533 in that region (Figure 3e). As a result, the *Ni* from homogeneous nucleation is

534 increased, which determines the increase in the Ni near 150 hPa over the west Pacific
535 Ocean due to the emission of aircraft soot (Figure 3a). Similarly, when the sulfur
536 emissions are increased from PI to PD, the change in cirrus clouds influences the
537 meteorological state. A large decrease in RH_i at 150hPa is found in the west Pacific
538 Ocean (Figure S4a), so that the occurrence frequency of homogeneous nucleation
539 decreases when sulfur emissions increase (Figure S4d). Additionally, the
540 temperature at 150hPa increases over the world (Figure S4b), which also contributes
541 partly to the decrease in the occurrence frequency of homogeneous nucleation.
542 Although global sulfur emissions increase sharply from PI (2.2 Tg S year⁻¹) to PD
543 (55 Tg S year⁻¹), the anthropogenic emissions mainly occur on the mainland with
544 much smaller emissions over the ocean even though the sulfur emissions from
545 shipping increase by 6.4 Tg S year⁻¹. The column number concentration of sulfate
546 having the potential to freeze homogeneously do not increase significantly over most
547 ocean regions (Figure S4c), so that the decrease in the occurrence frequency of
548 homogeneous nucleation leads to a decrease in Ni from homogeneous nucleation
549 over the west Pacific Ocean (Figure 4c). The increase in the temperature in the upper
550 troposphere over the world (Figure S4b) also partly explains the decrease in Ni from
551 heterogeneous nucleation when only sulfur emissions increase (Figure 4e). The
552 feedbacks to the meteorological state in remote regions always have an opposite
553 effect on the changes in Ni compared to the effect in regions with large
554 anthropogenic emissions. These meteorological feedbacks partly reduce the changes
555 in global average Ni due to anthropogenic emissions. Although these opposite
556 changes in Ni due to meteorological feedbacks are not statistically significant
557 (Figure 3a, 4a, 5a), our conjecture based on the model results indicates that the
558 meteorological feedbacks caused by the radiative effects of aerosols might
559 contribute to the change in Ni in remote regions. These important feedback processes
560 need to be investigated further.

561

562 3.2 Radiative forcing

563 The decrease in N_i in the upper troposphere usually leads to an increase in the
564 size of ice particles, which promotes the gravitational removal and formation of
565 snow, causing a decrease in the ice water path (IWP) and vice versa. As a result, the
566 change in IWP is mainly determined by the change in N_i and have a similar
567 geographic pattern. The global average IWP in the model is 14.6 g m^{-2} for the
568 PD_Base case, which is lower than that observed in different CloudSat/CALIPSO
569 analyses ($21\sim 28 \text{ g m}^{-2}$) (Li *et al.*, 2012). We used a cut off diameter of $250 \mu\text{m}$ to
570 move cloud ice to snow. A cutoff diameter of $400 \mu\text{m}$ in the model almost doubles
571 the IWP in our model (compare IWP of dbfc_mg10 and dbfc in Table 3 in Penner *et al.*,
572 2018). The emission of aircraft soot leads to a significant decrease in IWP in
573 Southeast Asia and the East coast of North America, caused by the inhibition of
574 homogeneous nucleation (Figure 6a). As shown in Figure 6b, the increase in the
575 sulfur emissions leads to a significant increase in IWP in the north Indian Ocean due
576 to the changes in N_i from homogeneous nucleation. The decrease in IWP in East
577 Asia and the Arctic is attributed to the decrease in N_i from heterogeneous nucleation
578 (Figure 6b). The geographic pattern of changes in IWP due to the change in all
579 anthropogenic emissions from PI to PD is dominated by the changes in IWP caused
580 by the changes in sulfur emissions (compare Figure 6b and 6c). However, the
581 increase in IWP in tropical regions is smaller and the decrease in IWP in the middle
582 and high latitudes of the NH is more negative in the PD_Base-PI_ALL case
583 compared to the PD_Base-PI_SO4 case because of the inhibition of homogeneous
584 nucleation caused by the increase in the emission of surface and aircraft soot. As a
585 result, although the geographical pattern of the changes in IWP is similar for the

586 PD_Base-PI_ALL and PD_Base-PI_SO4 cases, the magnitude of changes in the
587 global average IWP switches from positive (0.07 g m^{-2} for PD_Base-PI_SO4, Figure
588 6b) to negative (-0.13 g m^{-2} for PD_Base-PI_ALL, Figure 6c).

589 The changes in N_i and IWP lead to a change in the cirrus cloud fraction and also
590 feedback to produce a change in the lapse rate of temperature, which has an effect
591 on the delivery of water vapor and the strength of convection and these changes
592 influence the formation and lifetime of liquid water clouds. The liquid water path
593 (LWP) changes due to these complex dynamical feedbacks are shown in Figure S5.
594 The changes in global average LWP are all less than 0.5% with only a small number
595 of grids with a significant change. The changes in the shortwave and longwave
596 radiative fluxes are determined by the changes in LWP and IWP (as well as the
597 change in N_i), although they are dominated by the change in IWP. The changes in
598 aerosol only have a direct effect on the cirrus clouds in our model, while the changes
599 in warm clouds are caused by feedbacks due to the change in cirrus clouds. The
600 changes in the all-sky shortwave radiative forcing (SRF) and longwave radiative
601 forcing (LRF) at the top of the atmosphere (TOA) generally follow the changes in
602 IWP but have the opposite sign (Figure 7, Figure 8 and Figure 9). The changes in
603 LWP could either enhance or offset the effect of changes in IWP on the radiative
604 fluxes depending on whether the sign of the changes in IWP and LWP are
605 reinforcing or not. The emission of cSoot leads to a positive global average SRF due
606 to the significant increase in shortwave radiative fluxes off the coast of East Asia
607 and over the North Indian Ocean, while and the significant decrease in the longwave
608 radiative fluxes over East Asia, the North Indian Ocean and North Atlantic Ocean
609 contribute to a negative global average LRF mostly due to the decrease in the global
610 average IWP (Figure 7). On the other hand, the increase in sulfur emissions causes
611 a negative global average SRF largely due to the significant decrease over South

612 Asia, North Africa and the North Indian Ocean (Figure 8a). Simultaneously, the
613 increase in the IWP in these regions leads to a significant increase in longwave
614 radiative fluxes resulting in a positive global average LRF, although the LRF is
615 significantly negative in the middle to high latitude over the east coast of Asia.
616 (Figure 8b). The changes in the SRF and LRF due to the increase in all anthropogenic
617 emissions have a similar geographic pattern to those caused by the increase in sulfur
618 emissions but the global average forcings have opposite signs (compare Figure 8c,
619 8d and Figure 9c, 9d). This is due to the decrease in the global average IWP caused
620 by the inhibition of homogeneous nucleation as a result of the increased emissions
621 of soot.

622 The total all-sky net forcing (NRF) is determined by the balance between SRF
623 and LRF. The radiative effects in cirrus clouds are dominated by longwave radiative
624 effects. However, it is still possible that the radiative forcing due to changes in N_i in
625 cirrus clouds in some regions is dominated by SRF due to the combined effects on
626 shortwave forcing from the changes in cirrus clouds together with changes to warm
627 clouds caused by feedbacks. The emission of cSoot has a negative global average
628 NRF of $-0.14 \pm 0.07 \text{ W m}^{-2}$ in cirrus clouds with only a few significant grids, although
629 the SRF and LRF due to cSoot are significant in some coastal regions off of East and
630 South Asia (Figure 7). The NRF due to cSoot is most negative around the 30°N
631 where the emission of aircraft soot is high, while there is a small positive forcing
632 around 10°N dominated by SRF (Figure 7f). The NRF is the sum of the clear sky net
633 radiative forcing (NRFC) and the cloud radiative forcing (CRF) caused by changes
634 in cSoot. The global average CRF is $-0.10 \pm 0.07 \text{ W m}^{-2}$, which dominates over the
635 NRFC and explains 72% of the NRF of cSoot (Figure 7c, 7d).

636 Although the increase in sulfur emissions from PI to PD leads to an increase in
637 the global average N_i and IWP, the global average NRF due to sulfur emissions is

638 near zero, $-0.02 \pm 0.06 \text{ W m}^{-2}$. The NRF due to sulfur emissions is significant and
639 positive (up to 7.1 W m^{-2}) around the 30°N in South Asia and North Africa (Figure
640 8e). The NRF is negative over most mid to high latitudes of the NH, which is
641 attributed to the decrease in LRF associated with the feedback to the decrease in Ni
642 from heterogeneous nucleation there. However, the significant negative NRF in the
643 north Indian Ocean and positive NRF in the west Pacific Ocean are dominated by
644 the change in SRF (Figure 8a, 8e). The LWP increases in the north Indian Ocean as
645 a result of dynamic feedbacks from the changes in the cirrus clouds, leads to the
646 significant SRF together with the changes in IWP and cirrus clouds. The negative
647 NRF in the north Indian Ocean and mid to high latitudes of the NH offset the positive
648 NRF around the 30°N (Figure 8e). The significant negative NRF over the North
649 Indian Ocean is dominated by the CRF, while the significant positive NRF over
650 South Asia and North Africa is the combined effect of CRF and NRFC. The global
651 average CRF is $-0.17 \pm 0.06 \text{ W m}^{-2}$ and determines the sign of the global average NRF.
652 However, the global average NRFC is $0.14 \pm 0.02 \text{ W m}^{-2}$ with a wide area of positive
653 values over the NH, which offsets most of CRF.

654 Compared to the NRF due to the increased sulfur emissions, the NRF is less
655 positive in South Asia and more negative over the mid to high latitudes of the NH
656 and the north Indian Ocean when including the increased emissions of surface and
657 aircraft soot as well as sulfur together (Figure 9e). In the mid to high latitudes of the
658 Southern Hemisphere (SH), SRF and LRF always cancel each other so that NRF is
659 negligible. As a result, the global average NRF due to the all increased anthropogenic
660 emissions from PI to PD is $-0.20 \pm 0.05 \text{ W m}^{-2}$, which is mainly dominated by the
661 changes in LRF (Figure 9e, 9f). Both the CRF and NRFC due to all anthropogenic
662 emissions are largely explained by the CRF and NRFC caused by change in emission
663 of sulfur (compare Figure 9c, 9d and Figure 8c, 8d). The global average CRF is -

664 $0.28 \pm 0.04 \text{ W m}^{-2}$ due to the changes in all anthropogenic emissions, while the NRFC
665 is slightly positive ($0.08 \pm 0.02 \text{ W m}^{-2}$).

666

667 3.3 The influence of SOA on anthropogenic forcing

668 SOA particles have a strong potential to act as INPs and therefore influence the
669 formation of cirrus clouds. We examined the radiative forcing of all anthropogenic
670 aerosols on cirrus clouds when including the INPs from newly-nucleated SOA
671 particles. Figure 10 shows the column number concentration of INPs and zonal
672 average of INPs from SOA in the PD and PI atmosphere. Changes in natural SOA
673 precursors between the PI and PD atmospheres (i.e. isoprene, α -pinene and
674 limonene emissions) are caused by changes in temperature as well as by changes in
675 land-use, while changes in aromatic emissions are associated with anthropogenic
676 emission growth. In addition, newly formed SOA particles grow to accumulation
677 mode size as a result of coagulation of particles (sulfate and other newly formed
678 SOA particles), deposition of gaseous sulfate and incorporation of other SOA
679 compounds (e.g. through partitioning or kinetic uptake). Thus, the number
680 concentration of INPs from SOA is much higher in the PD than that in the PI due to
681 the much higher concentration of SOA in the accumulation mode in the PD (Zhu et
682 al., 2019). The INPs from SOA are highest in the middle latitude of the NH in the
683 PD, while the INPs from SOA are higher in the SH than that in the NH in the PI
684 atmosphere (Figure 10a, 10b). The INPs from SOA in the PD are spread between
685 600hPa to 150hPa with a peak around 300hPa, so there is a possible influence on the
686 formation of cirrus clouds (Figure 10b). The INPs from SOA in the PI have a peak
687 concentration that is a little higher than those in the PD (Figure 10d). The global
688 average N_i from heterogeneous nucleation increases by $1.86 \times 10^8 \text{ m}^{-2}$ from PI to PD

689 when including the INPs from SOA (Figure 11e), which is in contrast to the decrease
690 in the global average Ni from heterogeneous nucleation in the case without SOA
691 (Figure 5e). The INPs from SOA increase the Ni from heterogeneous nucleation in
692 both the PD and PI cases when compared to the PD_Base and PI_ALL cases (Figure
693 S6e, Figure S7e). However, the increase in Ni from heterogeneous nucleation in the
694 PD is much larger than that in the PI because of the larger number concentration of
695 INPs from SOA in the PD. As a result, the large increase in INPs from SOA between
696 the PD and the PI enhances heterogeneous nucleation resulting in an increase in Ni
697 from heterogeneous nucleation especially in the tropics around 150hPa and in
698 Antarctic from 400hPa to 200hPa (Figure 11f). The increase in the heterogeneous
699 nucleation when including SOA widely inhibits homogeneous nucleation in both the
700 PD and PI (Figure S6c, Figure S7c). In the PD, the increase in Ni from heterogeneous
701 nucleation even outweighs the decrease in Ni from homogeneous nucleation leading
702 to an increase of $0.4 \times 10^8 \text{ m}^{-2}$ in the global average Ni due to SOA compared to the
703 PD_Base case (Figure S6a). In contrast, the INPs from SOA in the PI case make a
704 larger contribution to the decrease in Ni from homogeneous nucleation than the
705 increase in Ni from heterogeneous nucleation resulting in a decrease in total Ni of -
706 $0.31 \times 10^8 \text{ m}^{-2}$ compared to the PI_ALL case (Figure S7a). The inclusion of INPs
707 from SOA decreases Ni in the tropics but increases Ni in the mid to high latitudes in
708 both the NH and SH (Figure S6b, S7b). The global average Ni in the PD increases
709 while the global average Ni in the PI is decreased. Both changes are caused by
710 additional INPs from SOA (Figure S6a, S7a) resulting in a larger increase in the
711 global average Ni from the PI to PD compared to the case without SOA (compare
712 Figure 5a and Figure 11a). When including INPs from SOA, Ni increases to a large
713 extent over south Asia, the north Indian Ocean and Antarctica due to the increase in
714 heterogeneous nucleation, while Ni decreases over the mid to high latitude of East
715 Asia and the North Pacific Ocean (compare Figure 11a and Figure 5a).

716 The increased N_i leads to a significant increase in the IWP in south Asia, the
717 north Indian Ocean and Antarctica due to the reduction of gravitational removal,
718 while the IWP decreases significantly in the mid to high latitude of East Asia which
719 is caused by the decrease in N_i (Figure 11a). Compared with the case without SOA
720 (PD_Base-PI_ALL), the inclusion of SOA increases the difference in the IWP
721 between the PD and PI in Antarctica significantly because of the increase in N_i from
722 heterogeneous nucleation of INPs from SOA there (Figure 12a). The change in the
723 LWP due to dynamic feedbacks in the case with SOA is significant in only a few
724 grids, which is similar to the case without SOA (Figure 12c). The larger increases in
725 N_i and IWP over South Asia and the north Indian Ocean lead to the larger changes
726 in both SRF and LRF when including SOA compared to the case without SOA, while
727 the significant decrease in N_i in the mid to high latitudes over East Asia leads to a
728 significant decrease in the LRF. The increase in N_i and IWP in Antarctica only
729 increases the LRF but does not change the SRF because of the very low shortwave
730 flux in polar regions (Figure 12c, 12d). The larger decrease in the SRF offsets the
731 increase in the LRF in the tropics when including SOA resulting in a similar value
732 for NRF in the tropics for the cases with and without SOA (Figure 13f). However,
733 the more positive changes in the LRF from PI to PD in Antarctica and the Arctic
734 when including SOA explain the more positive NRF there compared to the case
735 without SOA (Figure 13f). In addition, the NRF in south Asia and north Africa
736 around 30°N, where NRF is most positive in the case without SOA, becomes even
737 more positive when including SOA due to the larger increases in N_i . As a result, the
738 significant and larger positive NRF over Antarctica as well as south Asia and north
739 Africa around 30°N cause an increase in the global average NRF due to all
740 anthropogenic aerosol to $-0.04 \pm 0.08 \text{ W m}^{-2}$ when including SOA compared to the
741 value of $-0.20 \pm 0.05 \text{ W m}^{-2}$ in the case without SOA. The NRF when including SOA
742 is up to 6.6 W m^{-2} in the Arabian Peninsula while it is as low as -4.8 W m^{-2} in the

743 north Indian Ocean (Figure 12g). Compared to the case without SOA, the global
744 average CRF is less negative ($-0.14 \pm 0.07 \text{ W m}^{-2}$ compared to -0.28 W m^{-2}) largely
745 due to the significant positive CRF over Antarctica (Figure 12f). Simultaneously,
746 the NRFC is more positive in the case with SOA than the case without SOA, which
747 offset 73% of the CRF (Figure 12e).

748

749 **4. Conclusion and discussion**

750 This work develops a new ice nucleation parameterization, HYBRID, which is
751 a combination of the LP and KL parameterizations. The global model using this new
752 scheme is able to simulate the growth and decay of ice particles in the updrafts and
753 downdrafts associated with gravity waves as in the modified KL scheme (Penner et
754 al., 2018), and is able to treat the changes in aerosol number concentration from
755 freezing haze particles with fidelity in the sign of the change as in the LP scheme.
756 The HYBRID scheme overcomes some of the deficiencies in previous ice nucleation
757 schemes. We evaluated the HYBRID ice nucleation scheme by comparing the
758 scheme with the Liu and Penner (2005) adiabatic parcel model and by comparing its
759 global predictions using observed N_i . We used 10,000 parcel model simulations to
760 show that the HYBRID box model predicts 7.3% larger N_i than the LP adiabatic
761 parcel model with 21.5% larger N_i from homogeneous nucleation. The global model
762 using the HYBRID scheme overestimates N_i between 195K and 215K somewhat
763 compared to observations, as do earlier simulations with only the KL scheme
764 (Penner et al., 2018). The results of N_i from the HYBRID scheme are in reasonable
765 agreement with observations and thus were used in the CESM/IMPACT global
766 model to estimate the radiative forcing of aerosols in large-scale cirrus clouds. The
767 predicted N_i depends on the competition between homogeneous and heterogeneous
768 nucleation. These two ice nucleation processes dominate the formation of N_i in

769 different regions and altitudes. The global average Ni is dominated by homogeneous
770 nucleation in the PD atmosphere.

771 We performed a series of model experiments using the HYBRID ice nucleation
772 scheme to explore the forcing and cloud changes associated with changes in aircraft
773 soot, sulfur emissions and all anthropogenic emissions from the PI to PD. Results
774 are summarized in Table 3. The INPs from aircraft soot usually decrease Ni by the
775 inhibition of homogeneous nucleation in spite of some areas with small increases in
776 Ni . In contrast, the increase in sulfur emissions from PI to PD enhances
777 homogeneous nucleation in most regions and leads to a small decrease in the Ni
778 formed as a result of heterogeneous nucleation. We found that the effect of aerosols
779 in cirrus clouds could feedback to the meteorological state as determined by
780 temperature and RH_i, which could have an opposite effect on the changes in Ni due
781 to either aircraft soot or sulfur emissions in the remote regions like the west Pacific
782 Ocean. These meteorological feedbacks partly reduce the changes in the global
783 average Ni due to anthropogenic emissions. The changes in Ni from PI to PD caused
784 by all anthropogenic emissions are dominated by the changes due to the sulfur
785 emissions, but the changes in surface and aircraft soot emission have some effects
786 on the inhibition of homogeneous nucleation.

787 The changes in Ni due to anthropogenic aerosols lead to changes in IWP as
788 well as LWP due to dynamical feedbacks. The changes in SRF and LRF are always
789 determined by the changes in the IWP (and Ni), but the changes in LWP could either
790 enhance or offset the effects of IWP on the radiative fluxes. Emissions of aircraft
791 soot lead to a positive change in the global average SRF while the global average
792 LRF is negative. The changes in sulfur emissions from the PI to PD atmosphere
793 leads to opposite changes in the global average SRF and LRF compared to aircraft
794 soot because of the different signs of changes in Ni . The total net forcing in cirrus
795 clouds is usually dominated by LRF but it is dominated by SRF when the changes

796 in warm clouds cause a feedback that reinforces the effect of cirrus clouds on
797 shortwave fluxes. As a result, the emission of aircraft soot has a negative global
798 average NRF of $-0.14 \pm 0.07 \text{ W m}^{-2}$ in large-scale cirrus clouds, while the changes in
799 the sulfur emissions from the PI to the PD lead to a small negative global average
800 NRF of $-0.02 \pm 0.06 \text{ W m}^{-2}$. The global average NRF due to all anthropogenic
801 emissions from PI to PD, which is estimated to be $-0.20 \pm 0.05 \text{ W m}^{-2}$, is dominated
802 by the NRF caused by increased sulfur emissions but is more negative than the
803 forcing by sulfur emissions alone due to changes in the emissions of soot.

804 The influence of SOA on the anthropogenic forcing of aerosols in large-scale
805 cirrus clouds was examined. The additional INPs from SOA increase the N_i from
806 heterogeneous nucleation and decrease N_i from homogeneous nucleation, but the
807 sign of the changes in the total N_i depends on the balance of these two effects. The
808 high number concentration of INPs from SOA in the PD atmosphere causes an
809 increase in N_i compared to not including INPs from SOA while the low number
810 concentration in the PI atmosphere causes a decrease. As a result, the changes in N_i
811 due to the changes in anthropogenic emissions from PI to PD are larger when
812 including INPs from SOA than the case without SOA. The inclusion of SOA mainly
813 increases the changes in the NRF in the polar regions and the regions around 30°N ,
814 resulting in a less negative NRF of $-0.04 \pm 0.07 \text{ W m}^{-2}$ associated with the change in
815 all anthropogenic emissions.

816 The radiative forcing of anthropogenic aerosols effect on cirrus clouds estimated
817 in this study is less negative than the result indicated in Penner et al. (2009) (-0.38
818 to -0.56 W m^{-2}) and has a different sign compared with the result shown in Gettelman
819 et al. (2012) ($0.27 \pm 0.10 \text{ W m}^{-2}$). This is mostly caused by the different treatments
820 for updraft velocity, the concentration of haze particles, and INPs as well as the
821 application of a different ice nucleation scheme. Current models show that
822 homogeneous nucleation dominates the formation of new ice particles in most

823 regions over the world with the largest contribution to cirrus cloud formation in the
824 tropical upper troposphere (Zhou et al., 2016; Shi and Liu, 2018; Shi et al., 2015).
825 However, some observations indicated the importance and high occurrence
826 frequency of heterogeneous nucleation in the tropical tropopause region (Jensen et
827 al., 2013). Although the inclusion of INPs from newly formed SOA in this study
828 inhibits homogeneous nucleation in the tropics, homogeneous nucleation is still
829 responsible for 75% of total N_i in the PD atmosphere. Laboratory measurements
830 have supported other species acting as INP and enhancing heterogeneous nucleation
831 such as solid ammonium sulfate (Abbatt et al., 2006), which has not been considered
832 in current global climate models. Additional INPs from anthropogenic ammonium
833 sulfate can be expected to increase the anthropogenic forcing in cirrus clouds to be
834 less negative and possibly even positive. The HYBRID ice nucleation scheme
835 overestimates somewhat the ice number concentration produced from homogeneous
836 nucleation compared to a full parcel model. An explicit representation of the ice
837 nucleation process used in the global climate model may be helpful to predict the ice
838 number and therefore radiation budget more correctly in the future. The ability of
839 SOA to act as an INP probably varies depends on the property of different SOA
840 compounds as well as their particle size and mixing state (Baustian et al., 2013;
841 Berkemeier et al., 2014; Charnawskas et al., 2017; Shiraiwa et al., 2017). A global
842 climate model coupled online with the formation mechanism of SOA together with
843 an increased understanding of the ability of SOA to act as an INP would help in
844 estimating the contribution of SOA to ice particle formation more accurately.

845

846 **Code and data availability**

847 The latest version of CESM/IMPACT model and data used in this study are
848 available from the corresponding authors upon request.

849

850 **Author contribution**

851 JZ developed the model, performed the simulations, analyzed all data. JP guided
852 the model development and data analysis. Both authors contributed to writing the
853 paper.

854

855 **Competing interests**

856 The authors declare that they have no conflict of interest.

857

858 **Acknowledgments**

859 We are grateful to the reviewers and for funding from NSF-GEO grant number
860 1540954 and National Natural Science Foundation of China (Grant 41625014).
861 Computer time was provided by the NCAR CISL.

862

863 **References**

- 864 Abbatt, J., Benz, S., Cziczo, D., Kanji, Z., Lohmann, U., and Möhler, O.: Solid
865 ammonium sulfate aerosols as ice nuclei: A pathway for cirrus cloud formation,
866 *Science*, 313, 1770-1773, 2006.
- 867 Andreae, M. O., Afchine, A., Albrecht, R., Holanda, B. A., Artaxo, P., Barbosa, H.
868 M. J., Borrmann, S., Cecchini, M. A., Costa, A., Dollner, M., Fütterer, D., Järvinen,
869 E., Jurkat, T., Klimach, T., Konemann, T., Knote, C., Krämer, M., Krisna, T.,
870 Machado, L. A. T., Mertes, S., Minikin, A., Pöhlker, C., Pöhlker, M. L., Pöschl, U.,
871 Rosenfeld, D., Sauer, D., Schlager, H., Schnaiter, M., Schneider, J., Schulz, C.,
872 Spanu, A., Sperling, V. B., Voigt, C., Walser, A., Wang, J., Weinzierl, B., Wendisch,
873 M., and Ziereis, H.: Aerosol characteristics and particle production in the upper
874 troposphere over the Amazon Basin, *Atmospheric Chemistry and Physics*, 18, 921-
875 961, 10.5194/acp-18-921-2018, 2018.
- 876 Barahona, D., and Nenes, A.: Parameterization of cirrus cloud formation in large-
877 scale models: Homogeneous nucleation, *Journal of Geophysical Research:*
878 *Atmospheres*, 113, 2008.
- 879 Barrett, S., Prather, M., Penner, J., Selkirk, H., Balasubramanian, S., Doppelheuer, A.,
880 Fleming, G., Gupta, M., Halthore, R., and Hileman, J.: Guidance on the use of AEDT
881 gridded aircraft emissions in atmospheric models, A technical note submitted to the
882 US Federal Aviation Administration, Massachusetts Institute of Technology (MIT),
883 2010.
- 884 Baustian, K. J., Wise, M. E., Jensen, E. J., Schill, G. P., Freedman, M. A., and
885 Tolbert, M. A.: State transformations and ice nucleation in amorphous (semi-)solid
886 organic aerosol, *Atmospheric Chemistry and Physics*, 13, 5615-5628, 10.5194/acp-
887 13-5615-2013, 2013.
- 888 Berkemeier, T., Shiraiwa, M., Pöschl, U., and Koop, T.: Competition between water
889 uptake and ice nucleation by glassy organic aerosol particles, *Atmospheric*
890 *Chemistry and Physics*, 14, 12513-12531, 10.5194/acp-14-12513-2014, 2014.
- 891 Boville, B. A., P. J. Rasch, J. J. Hack, and J. R. McCaa: Representation of clouds
892 and precipitation processes in the Community Atmosphere Model version 3 (CAM3).
893 *J. Climate*, 19, 2184–2198, 2006.
- 894 Cantrell, W., and Heymsfield, A.: Production of ice in tropospheric clouds: A review,
895 *Bulletin of the American Meteorological Society*, 86, 795-808, 2005.

896 Charnawskas, J. C., Alpert, P. A., Lambe, A. T., Berkemeier, T., O'Brien, R. E.,
897 Massoli, P., Onasch, T. B., Shiraiwa, M., Moffet, R. C., Gilles, M. K., Davidovits,
898 P., Worsnop, D. R., and Knopf, D. A.: Condensed-phase biogenic-anthropogenic
899 interactions with implications for cold cloud formation, *Faraday Discuss*, 200, 165-
900 194, 10.1039/c7fd00010c, 2017.

901 Cziczo, D. J., Murphy, D. M., Hudson, P. K., and Thomson, D. S.: Single particle
902 measurements of the chemical composition of cirrus ice residue during CRYSTAL-
903 FACE, *Journal of Geophysical Research-Atmospheres*, 109, 10.1029/2003jd004032,
904 2004.Cziczo, D. J., Froyd, K. D., Hoose, C., Jensen, E. J., Diao, M., Zondlo, M. A.,
905 Smith, J. B., Twohy, C. H., and Murphy, D. M.: Clarifying the dominant sources
906 and mechanisms of cirrus cloud formation, *Science*, 340, 1320-1324, 2013.

907 DeMott, P., Cziczo, D., Prenni, A., Murphy, D., Kreidenweis, S., Thomson, D.,
908 Borys, R., and Rogers, D.: Measurements of the concentration and composition of
909 nuclei for cirrus formation, *Proceedings of the National Academy of Sciences*, 100,
910 14655-14660, 2003.

911 Fan, J., Wang, Y., Rosenfeld, D., and Liu, X.: Review of aerosol–cloud interactions:
912 Mechanisms, significance, and challenges, *Journal of the Atmospheric Sciences*, 73,
913 4221-4252, 2016.

914 Gary, B. L.: Mesoscale temperature fluctuations in the stratosphere, *Atmospheric*
915 *Chemistry and Physics*, 6, 4577-4589, 2006.

916 Gary, B. L.: Mesoscale temperature fluctuations in the Southern Hemisphere
917 stratosphere, *Atmospheric Chemistry and Physics*, 8, 4677-4681, 2008.

918 Gettelman, A., Liu, X., Barahona, D., Lohmann, U., and Chen, C.: Climate impacts
919 of ice nucleation, *Journal of Geophysical Research: Atmospheres*, 117,
920 10.1029/2012jd017950, 2012.

921 Gordon, H., Sengupta, K., Rap, A., Duplissy, J., Frege, C., Williamson, C., Heinritzi,
922 M., Simon, M., Yan, C., Almeida, J., Trostl, J., Nieminen, T., Ortega, I. K., Wagner,
923 R., Dunne, E. M., Adamov, A., Amorim, A., Bernhammer, A. K., Bianchi, F.,
924 Breitenlechner, M., Brilke, S., Chen, X., Craven, J. S., Dias, A., Ehrhart, S., Fischer,
925 L., Flagan, R. C., Franchin, A., Fuchs, C., Guida, R., Hakala, J., Hoyle, C. R.,
926 Jokinen, T., Junninen, H., Kangasluoma, J., Kim, J., Kirkby, J., Krapf, M., Kurten,
927 A., Laaksonen, A., Lehtipalo, K., Makhmutov, V., Mathot, S., Molteni, U., Monks,
928 S. A., Onnela, A., Perakyla, O., Piel, F., Petaja, T., Praplan, A. P., Pringle, K. J.,
929 Richards, N. A., Rissanen, M. P., Rondo, L., Sarnela, N., Schobesberger, S., Scott,
930 C. E., Seinfeld, J. H., Sharma, S., Sipila, M., Steiner, G., Stozhkov, Y., Stratmann,

931 F., Tome, A., Virtanen, A., Vogel, A. L., Wagner, A. C., Wagner, P. E., Weingartner,
932 E., Wimmer, D., Winkler, P. M., Ye, P., Zhang, X., Hansel, A., Dommen, J.,
933 Donahue, N. M., Worsnop, D. R., Baltensperger, U., Kulmala, M., Curtius, J., and
934 Carslaw, K. S.: Reduced anthropogenic aerosol radiative forcing caused by biogenic
935 new particle formation, *Proc Natl Acad Sci U S A*, 113, 12053-12058,
936 10.1073/pnas.1602360113, 2016.

937 Hendricks, J., Kärcher, B., and Lohmann, U.: Effects of ice nuclei on cirrus clouds
938 in a global climate model, *Journal of Geophysical Research*, 116,
939 10.1029/2010jd015302, 2011.

940 Hoesly, R. M., Smith, S. J., Feng, L., Klimont, Z., Janssens-Maenhout, G., Pitkanen,
941 T., Seibert, J. J., Vu, L., Andres, R. J., and Bolt, R. M.: Historical (1750–2014)
942 anthropogenic emissions of reactive gases and aerosols from the Community
943 Emissions Data System (CEDS), *Geoscientific Model Development (Online)*, 11,
944 2018.

945 Hong, Y., Liu, G. and Li, J. L.: Assessing the radiative effects of global ice clouds
946 based on CloudSat and CALIPSO measurements. *Journal of Climate*, 29(21), 7651-
947 7674, 2016.

948 Hoose, C., and Möhler, O.: Heterogeneous ice nucleation on atmospheric aerosols:
949 a review of results from laboratory experiments, *Atmospheric Chemistry and*
950 *Physics*, 12, 9817-9854, 10.5194/acp-12-9817-2012, 2012.

951 Ignatius, K., Kristensen, T. B., Jarvinen, E., Nihman, L., Fuchs, C., Gordon, H.,
952 Herenz, P., Hoyle, C. R., Duplissy, J., Garimella, S., Dias, A., Frege, C., Hoppel, N.,
953 Troestl, J., Wagner, R., Yan, C., Amorim, A., Baltensperger, U., Curtius, J.,
954 Donahue, N. M., Gallagher, M. W., Kirkby, J., Kulmala, M., Mohler, O., Saathoff,
955 H., Schnaiter, M., Tome, A., Virtanen, A., Worsnop, D., and Stratmann, F.:
956 Heterogeneous ice nucleation of viscous secondary organic aerosol produced from
957 ozonolysis of alpha-pinene, *Atmospheric Chemistry and Physics*, 16, 6495-6509,
958 10.5194/acp-16-6495-2016, 2016.

959 IPCC: *Climate Change 2013: The Physical Science Basis. Contribution of Working*
960 *Group I to the Fifth Assessment Report of the Intergovernmental Panel on Climate*
961 *Change*, Cambridge University Press, Cambridge, United Kingdom and New York,
962 NY, USA, 1535 pp., 2013.

963 Jensen, E. J., Diskin, G., Lawson, R. P., Lance, S., Bui, T. P., Hlavka, D., McGill,
964 M., Pfister, L., Toon, O. B., and Gao, R.: Ice nucleation and dehydration in the

965 Tropical Tropopause Layer, Proc Natl Acad Sci U S A, 110, 2041-2046,
966 10.1073/pnas.1217104110, 2013.

967 Joos, H., Spichtinger, P., Lohmann, U., Gayet, J. F., and Minikin, A.: Orographic
968 cirrus in the global climate model ECHAM5. Journal of Geophysical Research:
969 Atmospheres, 113(D18), 2008.

970 Kärcher, B., Hendricks, J., and Lohmann, U.: Physically based parameterization of
971 cirrus cloud formation for use in global atmospheric models, Journal of Geophysical
972 Research, 111, 10.1029/2005jd006219, 2006.

973 Kärcher, B., and Lohmann, U.: A parameterization of cirrus cloud formation:
974 Homogeneous freezing of supercooled aerosols, Journal of Geophysical Research:
975 Atmospheres, 107, AAC 4-1-AAC 4-10, 2002.

976 Knopf, D. A., Alpert, P. A., and Wang, B.: The Role of Organic Aerosol in
977 Atmospheric Ice Nucleation: A Review, ACS Earth and Space Chemistry, 2, 168-
978 202, 10.1021/acsearthspacechem.7b00120, 2018.

979 Koehler, K. A., DeMott, P. J., Kreidenweis, S. M., Popovicheva, O. B., Petters, M.
980 D., Carrico, C. M., Kireeva, E. D., Khokhlova, T. D., and Shonija, N. K.: Cloud
981 condensation nuclei and ice nucleation activity of hydrophobic and hydrophilic soot
982 particles, Physical Chemistry Chemical Physics, 11, 7906-7920, 2009.

983 Koop, T., Luo, B. P., Tsias, A., and Peter, T.: Water activity as the determinant for
984 homogeneous ice nucleation in aqueous solutions, Nature, 406, 611-614,
985 10.1038/35020537, 2000.

986 Koop, T., Bookhold, J., Shiraiwa, M., and Poschl, U.: Glass transition and phase
987 state of organic compounds: dependency on molecular properties and implications
988 for secondary organic aerosols in the atmosphere, Phys Chem Chem Phys, 13,
989 19238-19255, 10.1039/c1cp22617g, 2011.

990 Krämer, M., Schiller, C., Afchine, A., Bauer, R., Gensch, I., Mangold, A., Schlicht,
991 S., Spelten, N., Sitnikov, N., and Borrmann, S.: Ice supersaturations and cirrus cloud
992 crystal numbers, Atmospheric Chemistry and Physics, 9, 3505-3522, 2009.

993 Krämer, M., Rolf, C., Luebke, A., Afchine, A., Spelten, N., Costa, A., Meyer, J.,
994 Zoeger, M., Smith, J., and Herman, R. L.: A microphysics guide to cirrus clouds-
995 Part 1: Cirrus types, Atmospheric Chemistry and Physics, 16, 3463-3483, 2016.

996 Krämer, M., C. Rolf, N. Spelten, A. Afchine, D. Fahey, E. Jensen, S. Khaykin, T.
997 Kuhn, P. Lawson, and A. Lykov: A Microphysics Guide to Cirrus–Part II:
998 Climatologies of Clouds and Humidity from Observations, *Atmospheric Chemistry*
999 *and Physics Discussions*, doi:10.5194/acp-2020-40, 2020.

1000 Kuebbeler, M., Lohmann, U., Hendricks, J., and Kärcher, B.: Dust ice nuclei effects
1001 on cirrus clouds, *Atmos. Chem. Phys*, 14, 3027-3046, 2014.

1002 Kristjánsson, J. E., J. M. Edwards, and D. L. Mitchell: Impact of a new scheme for
1003 optical properties of ice crystals on climates of two gems. *J. Geophys. Res.*, 105, 10
1004 063–10 079, 2000.

1005 Li, J. L. F., Waliser, D. E., Chen, W. T., Guan, B., Kubar, T., Stephens, G., Ma, H.
1006 Y., Deng, M., Donner, L., Seman, C., and Horowitz, L.: An observationally based
1007 evaluation of cloud ice water in CMIP3 and CMIP5 GCMs and contemporary
1008 reanalyses using contemporary satellite data, *Journal of Geophysical Research-*
1009 *Atmospheres*, 117, 10.1029/2012jd017640, 2012.

1010 Liu, X., and Penner, J. E.: Ice nucleation parameterization for global models,
1011 *Meteorologische Zeitschrift*, 14, 499-514, 2005.Liu, X., Easter, R. C., Ghan, S. J.,
1012 Zaveri, R., Rasch, P., Shi, X., Lamarque, J. F., Gettelman, A., Morrison, H., Vitt, F.,
1013 Conley, A., Park, S., Neale, R., Hannay, C., Ekman, A. M. L., Hess, P., Mahowald,
1014 N., Collins, W., Iacono, M. J., Bretherton, C. S., Flanner, M. G., and Mitchell, D.:
1015 Toward a minimal representation of aerosols in climate models: description and
1016 evaluation in the Community Atmosphere Model CAM5, *Geoscientific Model*
1017 *Development*, 5, 709-739, 10.5194/gmd-5-709-2012, 2012.

1018 Liu, X., Penner, J. E., and Herzog, M.: Global modeling of aerosol dynamics: Model
1019 description, evaluation, and interactions between sulfate and nonsulfate aerosols,
1020 *Journal of Geophysical Research: Atmospheres*, 110, 2005.Liu, X., and Shi, X.:
1021 Sensitivity of homogeneous ice nucleation to aerosol perturbations and its
1022 implications for aerosol indirect effects through cirrus clouds, *Geophysical Research*
1023 *Letters*, 45, 1684-1691, 2018.

1024 Lohmann, U., von Salzen, K., McFarlane, N., Leighton, H. G., and Feichter, J.:
1025 Tropospheric sulfur cycle in the Canadian general circulation model, *Journal of*
1026 *Geophysical Research: Atmospheres*, 104, 26833-26858, 1999.

1027 Lohmann, U.: Possible aerosol effects on ice clouds via contact nucleation, *Journal*
1028 *of the atmospheric sciences*, 59, 647-656, 2002.

- 1029 Mahrt, F., Kilchhofer, K., Marcolli, C., Grönquist, P., David, R. O., Rösch, M.,
1030 Lohmann, U., and Kanji, Z. A.: The Impact of Cloud Processing on the Ice
1031 Nucleation Abilities of Soot Particles at Cirrus Temperatures, *Journal of*
1032 *Geophysical Research: Atmospheres*, 2019.
- 1033 Matus, A. V. and L'Ecuyer, T. S. : The role of cloud phase in Earth's radiation budget.
1034 *Journal of Geophysical Research: Atmospheres*, 122(5), 2559-2578, 2017.
- 1035 Pajunoja, A., Malila, J., Hao, L. Q., Joutsensaari, J., Lehtinen, K. E. J., and Virtanen,
1036 A.: Estimating the Viscosity Range of SOA Particles Based on Their Coalescence
1037 Time, *Aerosol Sci. Technol.*, 48, I-IV, 10.1080/02786826.2013.870325, 2014.
- 1038 Penner, J. E., Chen, Y., Wang, M., and Liu, X.: Possible influence of anthropogenic
1039 aerosols on cirrus clouds and anthropogenic forcing, *Atmospheric Chemistry and*
1040 *Physics*, 9, 879-896, 2009.
- 1041 Penner, J. E., Zhou, C., Garnier, A., and Mitchell, D. L.: Anthropogenic Aerosol
1042 Indirect Effects in Cirrus Clouds, *Journal of Geophysical Research: Atmospheres*,
1043 123, 11,652-611,677, 10.1029/2018jd029204, 2018.
- 1044 Podglajen, A., Hertzog, A., Plougonven, R., and Legras, B.: Lagrangian temperature
1045 and vertical velocity fluctuations due to gravity waves in the lower stratosphere,
1046 *Geophysical Research Letters*, 43, 3543-3553, 2016.
- 1047 Pratt, K., Murphy, S., Subramanian, R., DeMott, P., Kok, G., Campos, T., Rogers,
1048 D., Prenni, A., Heymsfield, A., and Seinfeld, J.: Flight-based chemical
1049 characterization of biomass burning aerosols within two prescribed burn smoke
1050 plumes, *Atmospheric Chemistry and Physics*, 11, 12549-12565, 2011.
- 1051 Prenni, A. J., DeMott, P. J., Sullivan, A. P., Sullivan, R. C., Kreidenweis, S. M., and
1052 Rogers, D. C.: Biomass burning as a potential source for atmospheric ice nuclei:
1053 Western wildfires and prescribed burns, *Geophysical Research Letters*, 39, 2012.
- 1054 Renbaum-Wolff, L., Grayson, J. W., Bateman, A. P., Kuwata, M., Sellier, M.,
1055 Murray, B. J., Shilling, J. E., Martin, S. T., and Bertram, A. K.: Viscosity of alpha-
1056 pinene secondary organic material and implications for particle growth and
1057 reactivity, *Proc. Natl. Acad. Sci. U. S. A.*, 110, 8014-8019,
1058 10.1073/pnas.1219548110, 2013.
- 1059 Richardson, M. S., DeMott, P. J., Kreidenweis, S. M., Cziczo, D. J., Dunlea, E. J.,
1060 Jimenez, J. L., Thomson, D. S., Ashbaugh, L. L., Borys, R. D., Westphal, D. L.,
1061 Casuccio, G. S., and Lersch, T. L.: Measurements of heterogeneous ice nuclei in the

1062 western United States in springtime and their relation to aerosol characteristics,
1063 *Journal of Geophysical Research-Atmospheres*, 112, 10.1029/2006jd007500, 2007.

1064 Saukko, E., Lambe, A. T., Massoli, P., Koop, T., Wright, J. P., Croasdale, D. R.,
1065 Pedernera, D. A., Onasch, T. B., Laaksonen, A., Davidovits, P., Worsnop, D. R., and
1066 Virtanen, A.: Humidity-dependent phase state of SOA particles from biogenic and
1067 anthropogenic precursors, *Atmospheric Chemistry and Physics*, 12, 7517-7529,
1068 10.5194/acp-12-7517-2012, 2012.

1069 Shi, X., Liu, X., and Zhang, K.: Effects of pre-existing ice crystals on cirrus clouds
1070 and comparison between different ice nucleation parameterizations with the
1071 Community Atmosphere Model (CAM5), *Atmospheric Chemistry and Physics*, 15,
1072 1503-1520, 10.5194/acp-15-1503-2015, 2015.

1073 Shi, X., and Liu, X.: Sensitivity Study of Anthropogenic Aerosol Indirect Forcing
1074 through Cirrus Clouds with CAM5 Using Three Ice Nucleation Parameterizations,
1075 *Journal of Meteorological Research*, 32, 693-706, 10.1007/s13351-018-8011-z,
1076 2018.

1077 Shiraiwa, M., Li, Y., Tsimpidi, A. P., Karydis, V. A., Berkemeier, T., Pandis, S. N.,
1078 Lelieveld, J., Koop, T., and Pöschl, U.: Global distribution of particle phase state in
1079 atmospheric secondary organic aerosols, *Nature Communications*, 8, 15002,
1080 10.1038/ncomms15002, 2017.

1081 Storelvmo, T.: Aerosol Effects on Climate via Mixed-Phase and Ice Clouds, *Annual*
1082 *Review of Earth and Planetary Sciences*, 45, 199-222, 10.1146/annurev-earth-
1083 060115-012240, 2017.

1084 Tilmes, S., Lamarque, J.-F., Emmons, L. K., Kinnison, D. E., Marsh, D., Garcia, R.
1085 R., Smith, A. K., Neely, R. R., Conley, A., Vitt, F., Val Martin, M., Tanimoto, H.,
1086 Simpson, I., Blake, D. R., and Blake, N.: Representation of the Community Earth
1087 System Model (CESM1) CAM4-chem within the Chemistry-Climate Model
1088 Initiative (CCMI), *Geoscientific Model Development*, 9, 1853-1890, 10.5194/gmd-
1089 9-1853-2016, 2016.

1090 van Marle, M. J. E., Kloster, S., Magi, B. I., Marlon, J. R., Daniau, A.-L., Field, R.
1091 D., Arneth, A., Forrest, M., Hantson, S., Kehrwald, N. M., Knorr, W., Lasslop, G.,
1092 Li, F., Mangeon, S., Yue, C., Kaiser, J. W., and van der Werf, G. R.: Historic global
1093 biomass burning emissions for CMIP6 (BB4CMIP) based on merging satellite
1094 observations with proxies and fire models (1750–2015), *Geoscientific Model*
1095 *Development*, 10, 3329-3357, 10.5194/gmd-10-3329-2017, 2017.

- 1096 Wagner, R., Höhler, K., Huang, W., Kiselev, A., Möhler, O., Mohr, C., Pajunoja, A.,
1097 Saathoff, H., Schiebel, T., Shen, X., and Virtanen, A.: Heterogeneous ice nucleation
1098 of α -pinene SOA particles before and after ice cloud processing, *Journal of*
1099 *Geophysical Research: Atmospheres*, 122, 4924-4943, 10.1002/2016jd026401,
1100 2017.
- 1101 Waliser, D. E., Li, J. L. F., Woods, C. P., Austin, R. T., Bacmeister, J., Chern, J.,
1102 Del Genio, A., Jiang, J. H., Kuang, Z., and Meng, H.: Cloud ice: A climate model
1103 challenge with signs and expectations of progress, *Journal of Geophysical Research:*
1104 *Atmospheres*, 114, 2009.
- 1105 Wang, B., Lambe, A. T., Massoli, P., Onasch, T. B., Davidovits, P., Worsnop, D. R.,
1106 and Knopf, D. A.: The deposition ice nucleation and immersion freezing potential
1107 of amorphous secondary organic aerosol: Pathways for ice and mixed-phase cloud
1108 formation, *Journal of Geophysical Research: Atmospheres*, 117, 2012.
- 1109 Wang, M., Liu, X., Zhang, K., and Comstock, J. M.: Aerosol effects on cirrus
1110 through ice nucleation in the Community Atmosphere Model CAM5 with a
1111 statistical cirrus scheme, *Journal of Advances in Modeling Earth Systems*, 6, 756-
1112 776, 10.1002/2014ms000339, 2014. Wang, M., and Penner, J. E.: Aerosol indirect
1113 forcing in a global model with particle nucleation, *Atmospheric Chemistry and*
1114 *Physics*, 9, 239-260, 2009.
- 1115 Wang, M., and Penner, J. E.: Cirrus clouds in a global climate model with a statistical
1116 cirrus cloud scheme, *Atmospheric Chemistry and Physics*, 10, 5449-5474,
1117 10.5194/acp-10-5449-2010, 2010.
- 1118 Wang, P. H., Minnis, P., McCormick, M. P., Kent, G. S., and Skeens, K. M.: A 6-
1119 year climatology of cloud occurrence frequency from Stratospheric Aerosol and Gas
1120 Experiment II observations (1985 – 1990), *Journal of Geophysical Research:*
1121 *Atmospheres*, 101, 29407-29429, 1996.
- 1122 Wilson, T. W., Murray, B. J., Wagner, R., Möhler, O., Saathoff, H., Schnaiter, M.,
1123 Skrotzki, J., Price, H. C., Malkin, T. L., Dobbie, S., and Al-Jumur, S. M. R. K.:
1124 Glassy aerosols with a range of compositions nucleate ice heterogeneously at cirrus
1125 temperatures, *Atmospheric Chemistry and Physics*, 12, 8611-8632, 10.5194/acp-12-
1126 8611-2012, 2012.
- 1127 Wilkerson, J. T., Jacobson, M. Z., Malwitz, A., Balasubramanian, S., Wayson, R.,
1128 Fleming, G., Naiman, A. D., and Lele, S. K.: Analysis of emission data from global

1129 commercial aviation: 2004 and 2006, *Atmos. Chem. Phys.*, 10, 6391–6408,
1130 <https://doi.org/10.5194/acp-10-6391-2010>, 2010.

1131 Yun, Y., Penner, J. E., and Popovicheva, O.: The effects of hygroscopicity on ice
1132 nucleation of fossil fuel combustion aerosols in mixed-phase clouds, *Atmospheric*
1133 *Chemistry and Physics*, 13, 4339-4348, 10.5194/acp-13-4339-2013, 2013.

1134 Zender, C. S., Bian, H., and Newman, D.: Mineral Dust Entrainment and Deposition
1135 (DEAD) model: Description and 1990s dust climatology, *Journal of Geophysical*
1136 *Research: Atmospheres*, 108, 2003.

1137 Zhang, K., Wan, H., Liu, X., Ghan, S. J., Kooperman, G. J., Ma, P.-L., Rasch, P. J.,
1138 Neubauer, D., and Lohmann, U.: On the use of nudging for aerosol–climate model
1139 intercomparison studies, *Atmospheric Chemistry and Physics*, 14, 8631-8645, 2014.

1140 Zhou, C., and Penner, J. E.: Aircraft soot indirect effect on large-scale cirrus clouds:
1141 Is the indirect forcing by aircraft soot positive or negative?, *Journal of Geophysical*
1142 *Research-Atmospheres*, 119, 11303-11320, 10.1002/2014jd021914, 2014.

1143 Zhou, C., Penner, J. E., Lin, G., Liu, X., and Wang, M.: What controls the low ice
1144 number concentration in the upper troposphere?, *Atmospheric Chemistry and*
1145 *Physics*, 16, 12411-12424, 10.5194/acp-16-12411-2016, 2016.

1146 Zhu, J., and Penner, J. E.: Global Modeling of Secondary Organic Aerosol With
1147 Organic Nucleation, *Journal of Geophysical Research: Atmospheres*, 124, 8260-
1148 8286, 2019.

1149 Zhu, J., and Penner, J. E.: Indirect effects of secondary organic aerosol on cirrus
1150 clouds, *Journal of Geophysical Research: Atmospheres*, 10.1029/2019JD032233,
1151 2020.

1152 Zhu, J., Penner, J. E., Lin, G., Zhou, C., Xu, L., and Zhuang, B.: Mechanism of SOA
1153 formation determines magnitude of radiative effects, *Proc Natl Acad Sci U S A*, 114,
1154 12685-12690, 10.1073/pnas.1712273114, 2017.

1155 Zhu, J., Penner, J. E., Yu, F., Sillman, S., Andreae, M. O., and Coe, H.: Decrease in
1156 radiative forcing by organic aerosol nucleation, climate, and land use change, *Nature*
1157 *Communications*, 10, 423, 10.1038/s41467-019-08407-7, 2019.

1158

1159

1160

1161 **Tables**

1162 Table 1. Summary of assumptions for aerosols to be effective INPs in the model

Aerosol component	Assumption to be effective INPs
Fossil/bio-fuel OM/BC	0.05% of fSoot with <1 monolayers of sulfate and 0.1% with 1-3 monolayers of sulfate when RH _i reaches 120%
Biomass OM/BC	0.1% of bSoot when RH _i reaches 120%
Aircraft OM/BC	Pre-activated aircraft soot within contrails with less than 3 monolayers of sulfate when RH _i reaches 120%
Dust	Dust with fewer than 3 monolayers of sulfate coating when RH _i reaches 120%
SOA	The newly formed SOA grow to the accumulation mode and meets the requirements of the glass transition temperature and RH _i calculated using the equations in Wang et al. (2012) when RH _i reaches 120%

1163

1164 Table 2. Description of cases

Case name	Description
PD_Base	Emissions for the present day (≈ 2000) for anthropogenic sulfur, surface and aircraft soot
PI_cSoot	As in PD_Base without INPs from pre-activated aircraft soot in contrails
PI_SO4	As in PD_Base, but with the anthropogenic sulfur emission for the preindustrial period (≈ 1750)
PI_ALL	As in PD_Base, but with the anthropogenic sulfur emission and surface soot emission for the pre-industrial period (≈ 1750) and without aircraft soot
PD_SOA	As in PD_Base, but adding INPs from newly formed SOA particles in present day
PI_SOA	As in PI_ALL, but adding INPs from newly formed SOA particles in preindustrial period

1165 Note: SOA=secondary organic aerosol; INP=ice nucleating particle.

1166

1167 Table 3. Forcing and cloud changes associated with changes in aircraft soot, sulfur
 1168 and all anthropogenic aerosols.

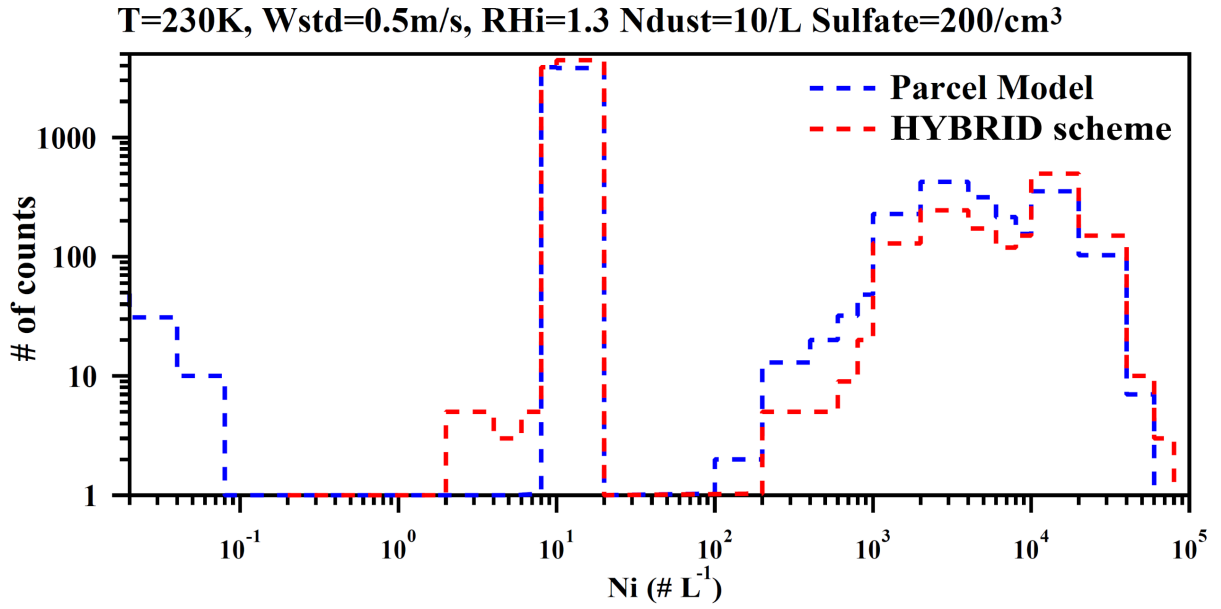
Parameter	PD_Base-PI_cSoot	PD_Base-PI_SO4	PD_Base-PI_ALL	PD_SOA-PI_SOA
Ni (10^7 m^{-2})	-1.00±2.40	<i>7.26±2.88</i>	4.93±1.80	<i>11.96±2.29</i>
IWP (g m^{-2})	-0.13±0.06	0.07±0.06	-0.13±0.04	-0.12±0.05
LWP (g m^{-2})	-0.19±0.04	0.16±0.07	-0.05±0.08	0.03±0.06
SRF (W m^{-2})	0.35±0.13	-0.36±0.10	0.10±0.06	-0.14±0.11
LRF (W m^{-2})	<i>-0.49±0.09</i>	<i>0.33±0.05</i>	<i>-0.30±0.06</i>	0.10±0.04
NRF (W m^{-2})	-0.14±0.07	-0.02±0.06	-0.20±0.05	-0.04±0.08

1169 Note: Differences significant at the 90% level according to a Student's t test are
 1170 italic.

1171

1172 **Figures**

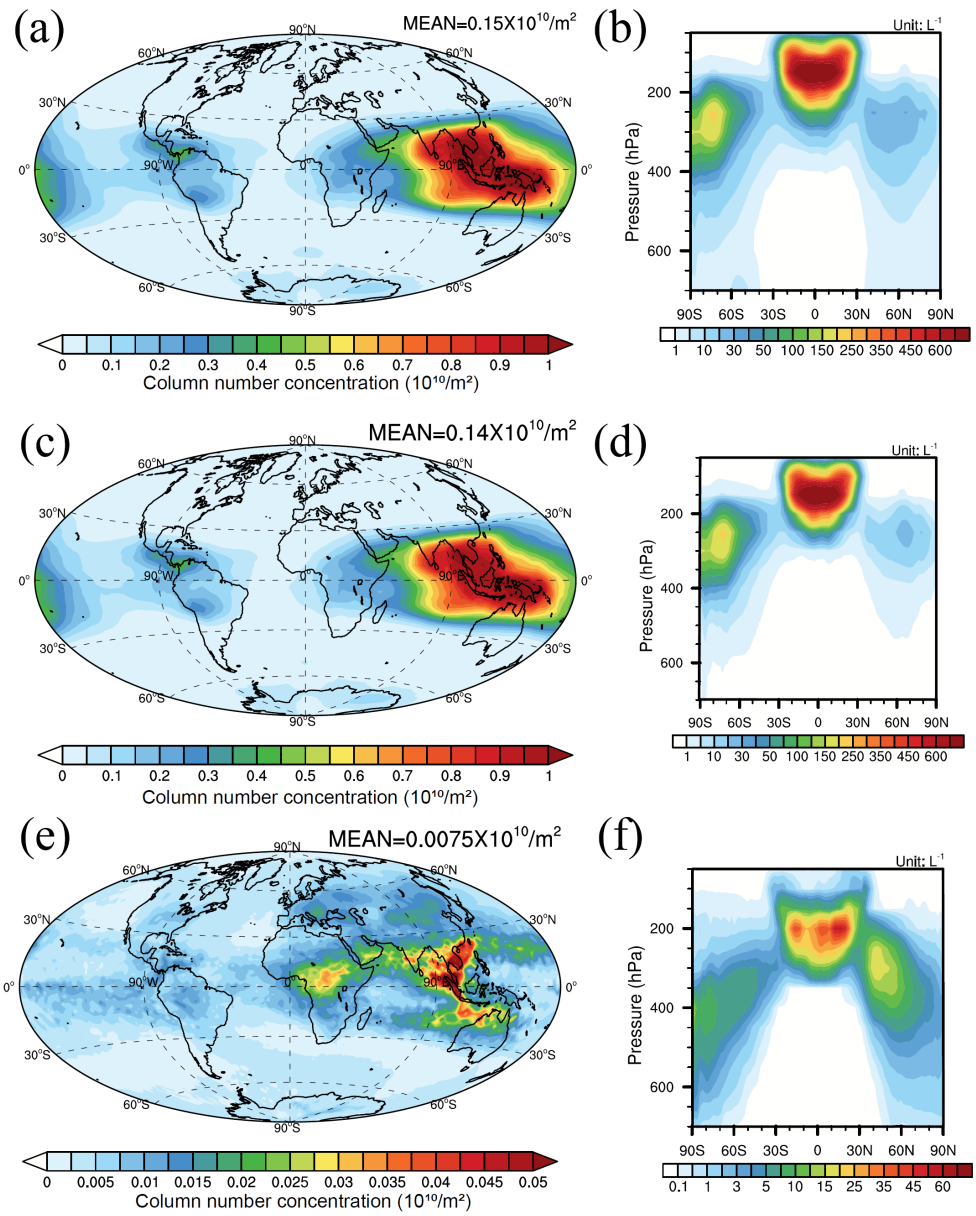
1173



1174

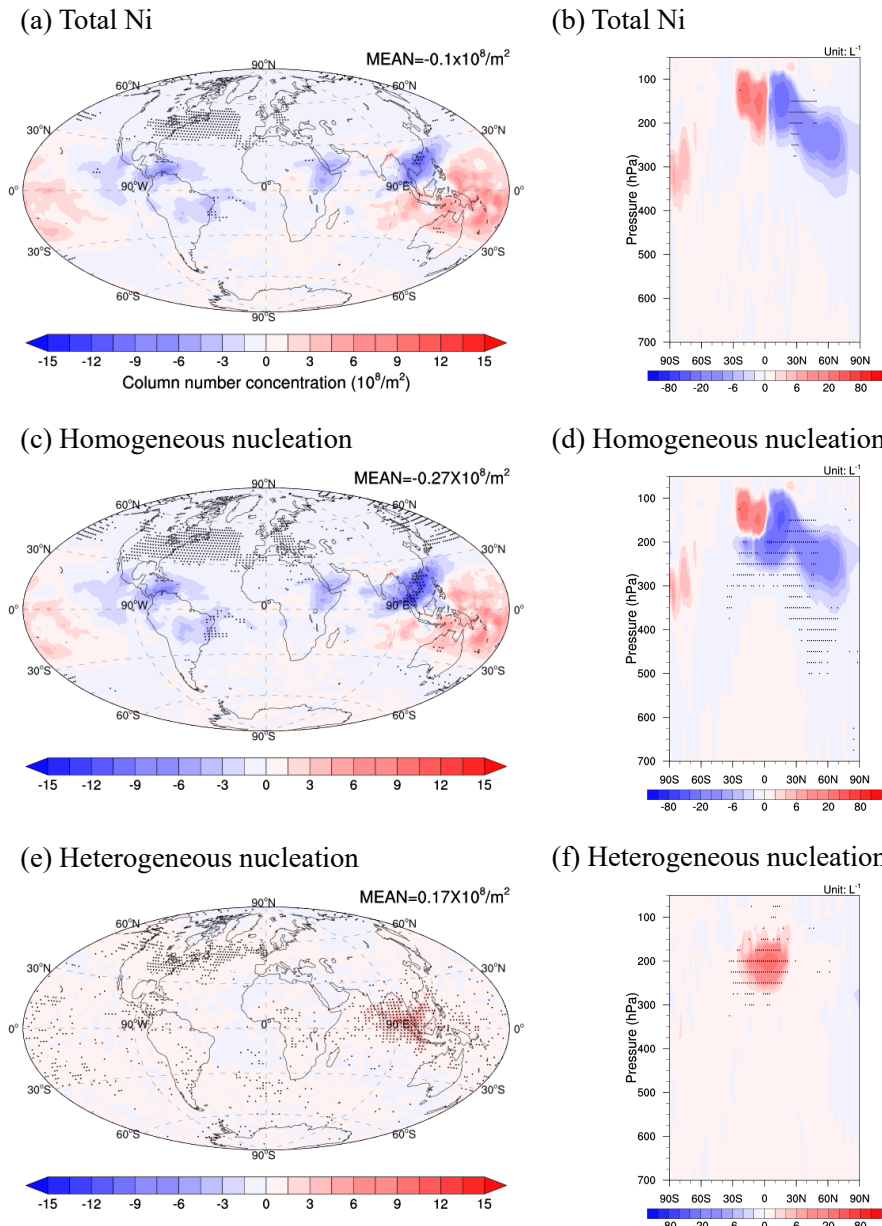
1175 Figure 1. Histogram of predicted ice number concentration for 10,000 simulations
1176 using an adiabatic parcel model (blue dashed line) and a box model using the
1177 HYBRID scheme (red dashed line). Wstd is the standard deviation of the assumed
1178 pdf of updraft velocities, while Ndust and Sulfate are the assumed dust and sulfate
1179 number concentrations.

1180



1182

1183 Figure 2. The vertically integrated total Ni in PD_Base case (a), Ni from
 1184 homogeneous nucleation (c) and Ni from heterogeneous nucleation (e). The zonal
 1185 average plots of Ni in PD_Base case (b), Ni from homogeneous nucleation (d) and
 1186 Ni from heterogeneous nucleation (f). Note: the vertical axis in (b), (d) and (f) are
 1187 in hybrid pressure levels

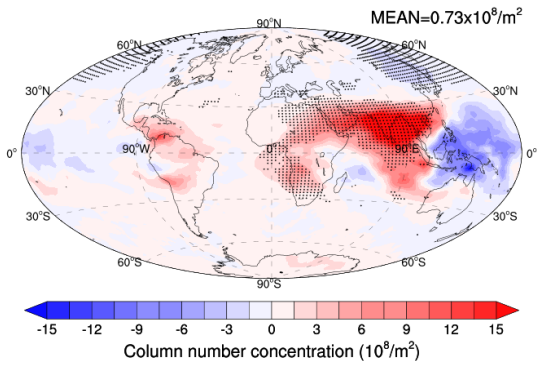


1188

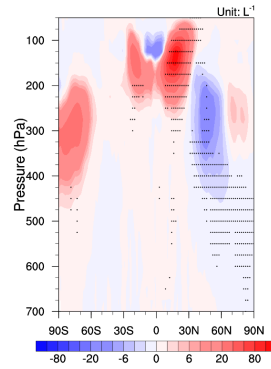
1189 Figure 3. The annual average change in column number concentration (a, c, e) and
 1190 zonal average number concentration (b, d, f) of total ice (a, b), ice from
 1191 homogeneous nucleation (c, d) and ice from heterogeneous nucleation (e, f) for the
 1192 difference between the PD_Base and PI_cSoot cases. Differences significant at the
 1193 90% level according to a Student's t test are depicted by points.

1194

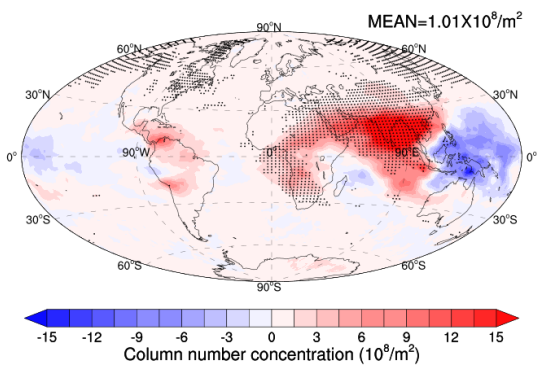
(a) Total Ni



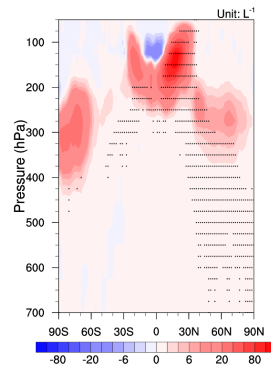
(b) Total Ni



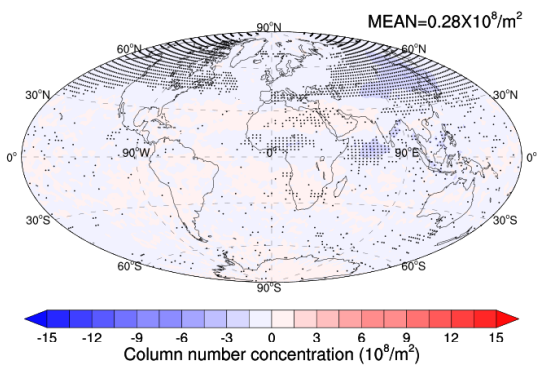
(c) Homogeneous nucleation



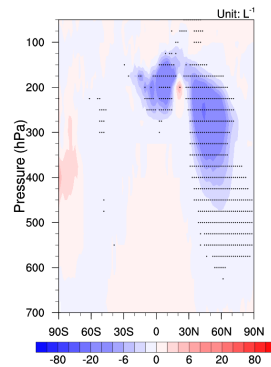
(d) Homogeneous nucleation



(e) Heterogeneous nucleation



(f) Heterogeneous nucleation



1195

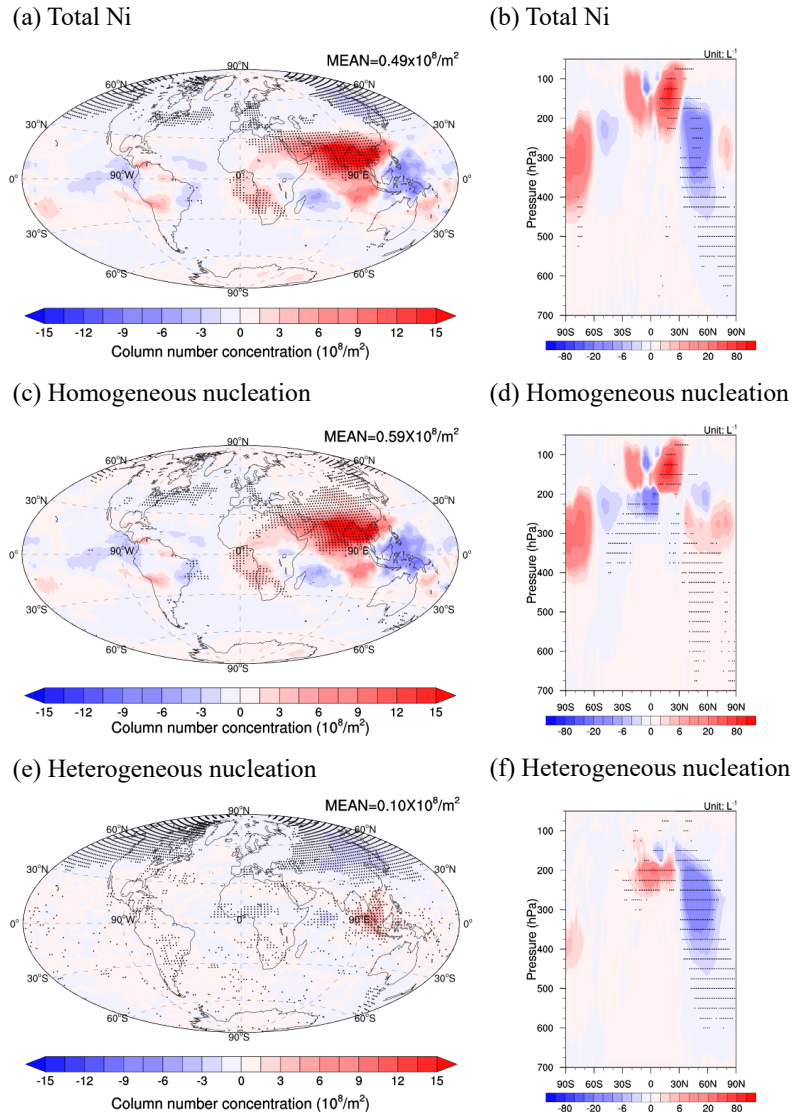
1196 Figure 4. As in Figure 3 but for the difference between the PD_Base and PI_SO4

1197 cases. Differences significant at the 90% level according to a Student's t test are

1198 depicted by points.

1199

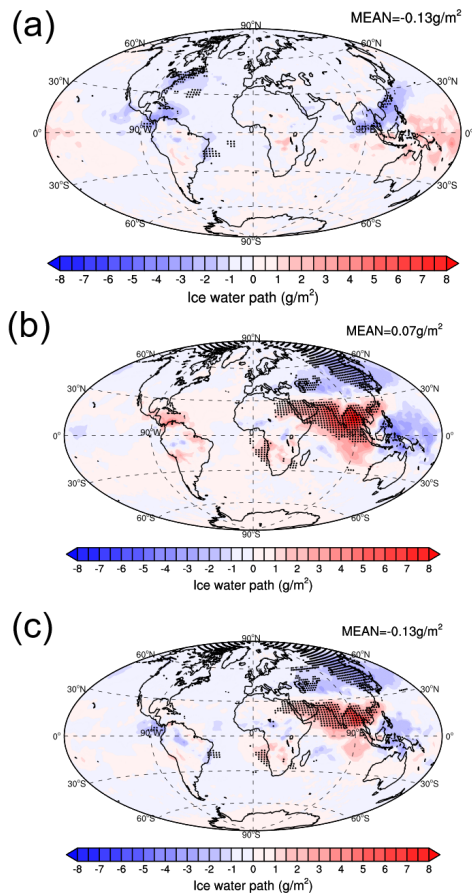
1200



1201

1202 Figure 5. As in Figure 3 but for the difference between the PD_Base and PI_ALL
 1203 cases. Differences significant at the 90% level according to a Student's t test are
 1204 depicted by points.

1205

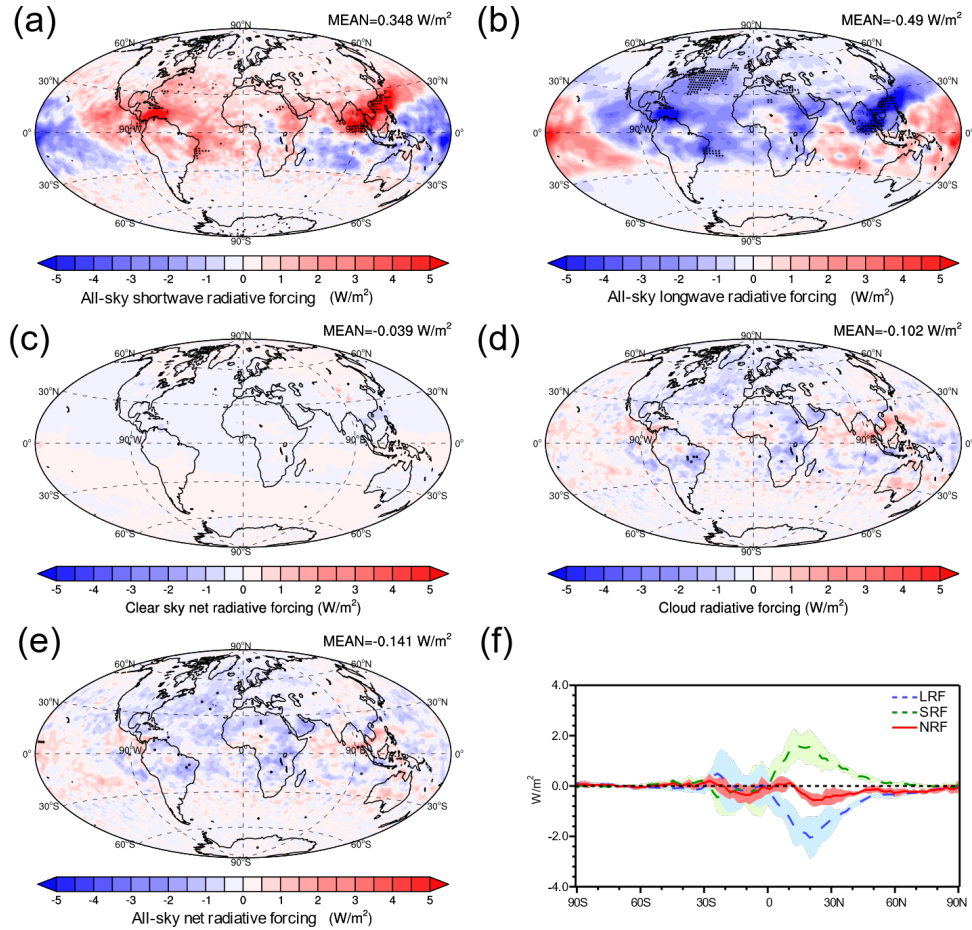


1206

1207 Figure 6. Annual mean plots of the change in vertically integrated averaged ice
 1208 water path for the difference between the PD_Base and PI_cSoot cases (a),
 1209 PD_Base and PI_SO4 cases (b) as well as the PD_Base and PI_ALL cases (c).

1210 Differences significant at the 90% level according to a Student's t test are depicted
 1211 by points.

1212

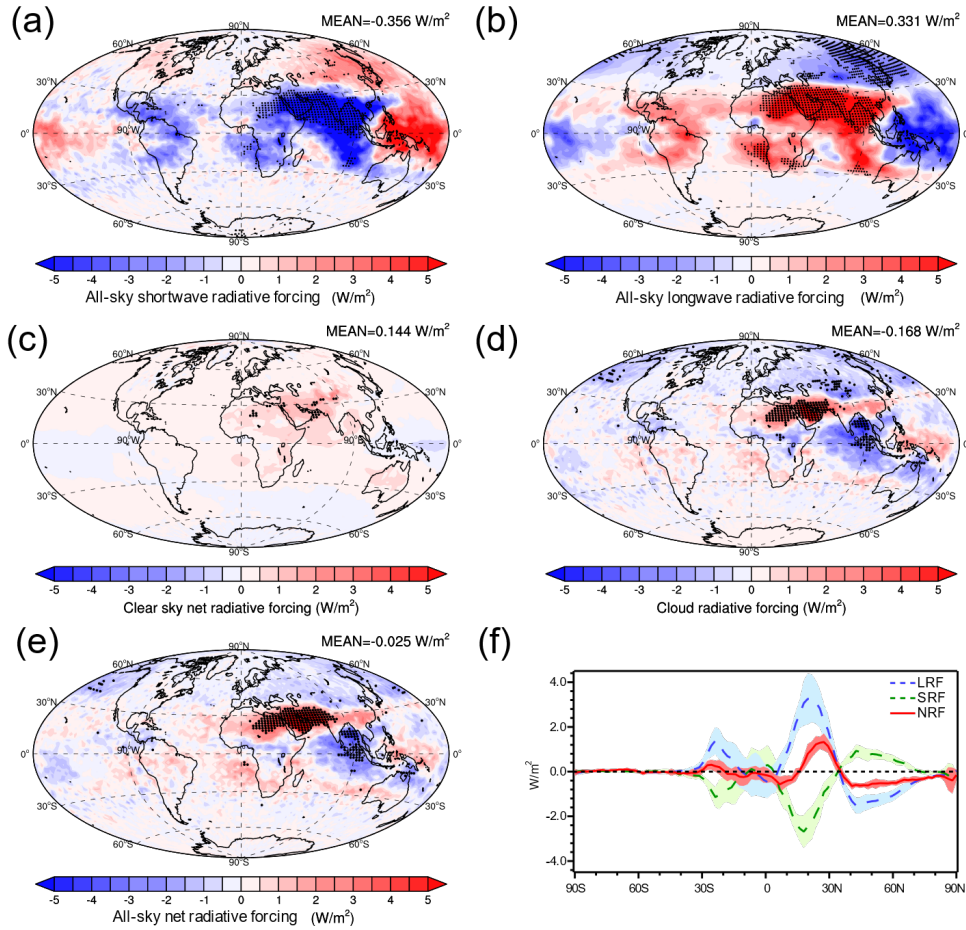


1213

1214 Figure 7. Annual mean plots of all-sky shortwave radiative forcing (a), all-sky
 1215 longwave radiative forcing (b), clear sky net radiative forcing (c), cloud radiative
 1216 forcing (d) and all-sky net radiative forcing (e) as well as all-sky longwave
 1217 radiative forcing (f, LRF, blue dashed line), all-sky shortwave radiative forcing (f,
 1218 SRF, green dashed line) and all-sky net radiative forcing (f, NRF, red solid line)
 1219 versus latitude for the difference between the PD_Base and PI_cSoot cases.

1220 Differences significant at the 90% level according to a Student's t test are depicted
 1221 by points. The shading in (f) represents one standard deviation of the interannual
 1222 variation over six years.

1223

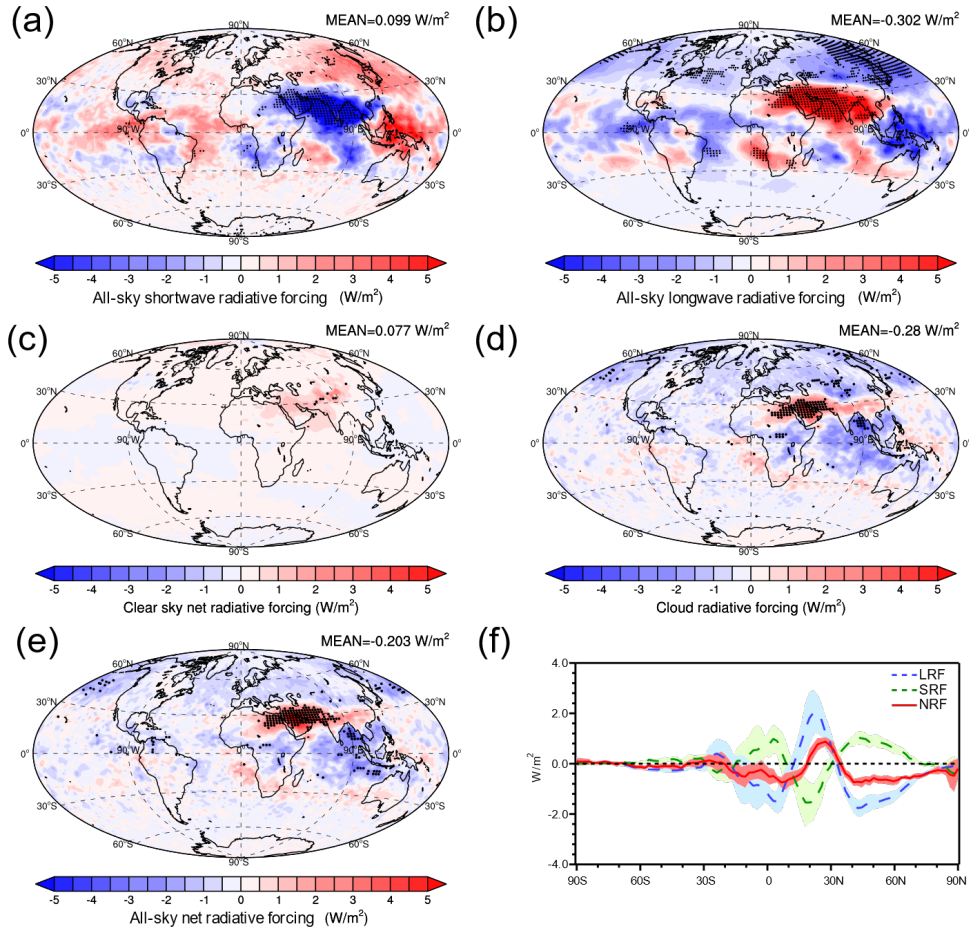


1224

1225 Figure 8. As in Figure 7 but for the difference between the PD_Base and PI_SO4
 1226 cases. Differences significant at the 90% level according to a Student's t test are
 1227 depicted by points. The shading in (f) represents one standard deviation of the
 1228 interannual variation over six years.

1229

1230



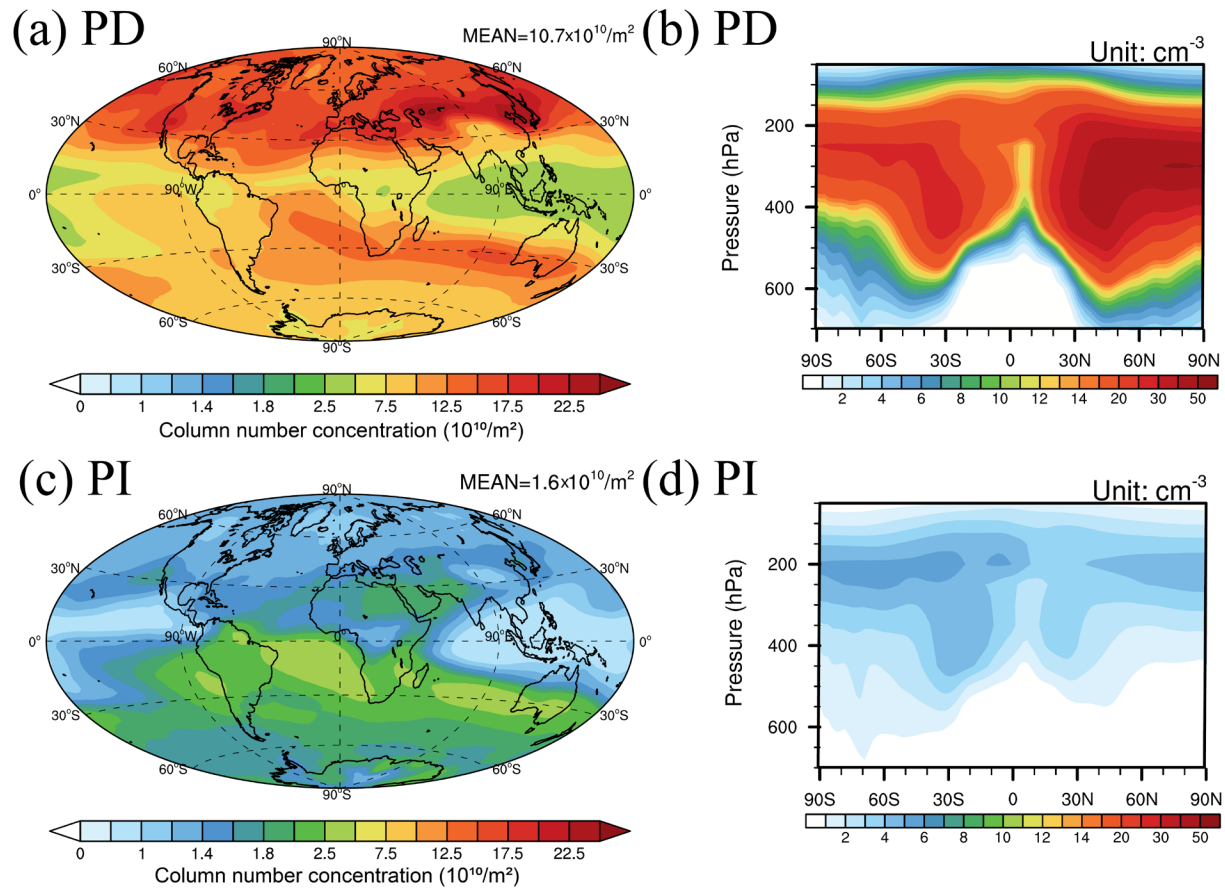
1231

1232 Figure 9. As in Figure 7 but for the difference between the PD_Base and PI_ALL
 1233 cases. Differences significant at the 90% level according to a Student's t test are
 1234 depicted by points. The shading in (f) represents one standard deviation of the
 1235 interannual variation over six years.

1236

1237

1238



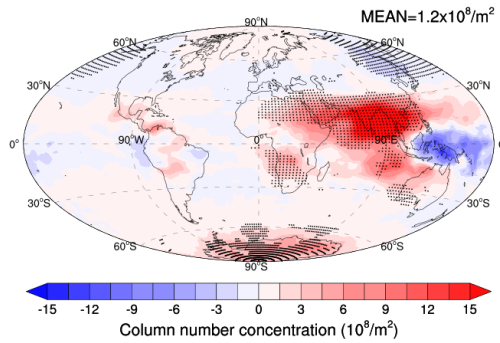
1239

1240 Figure 10. The vertically integrated number of INP (a, c) and zonal average plots
 1241 of INP (b, d) from SOA in the PD_SOA (a, b) and PI_SOA (c, d) cases.

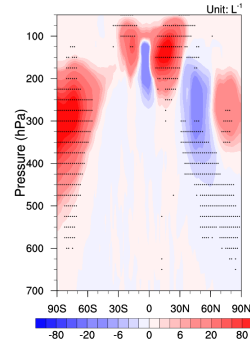
1242

1243

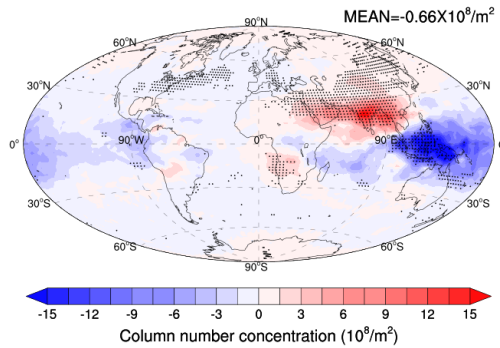
(a) Total Ni



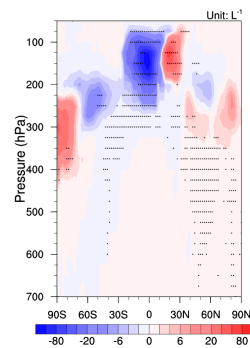
(b) Total Ni



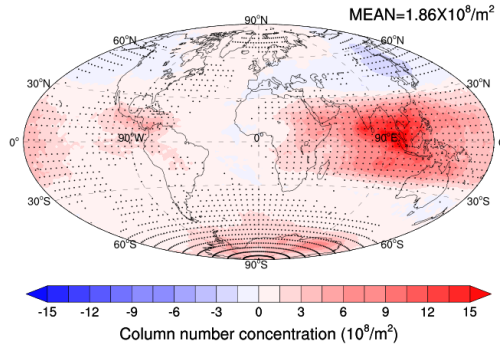
(c) Homogeneous nucleation



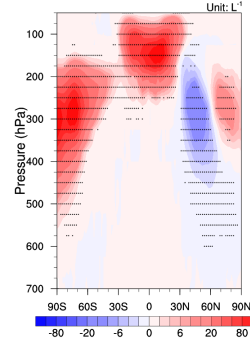
(d) Homogeneous nucleation



(e) Heterogeneous nucleation



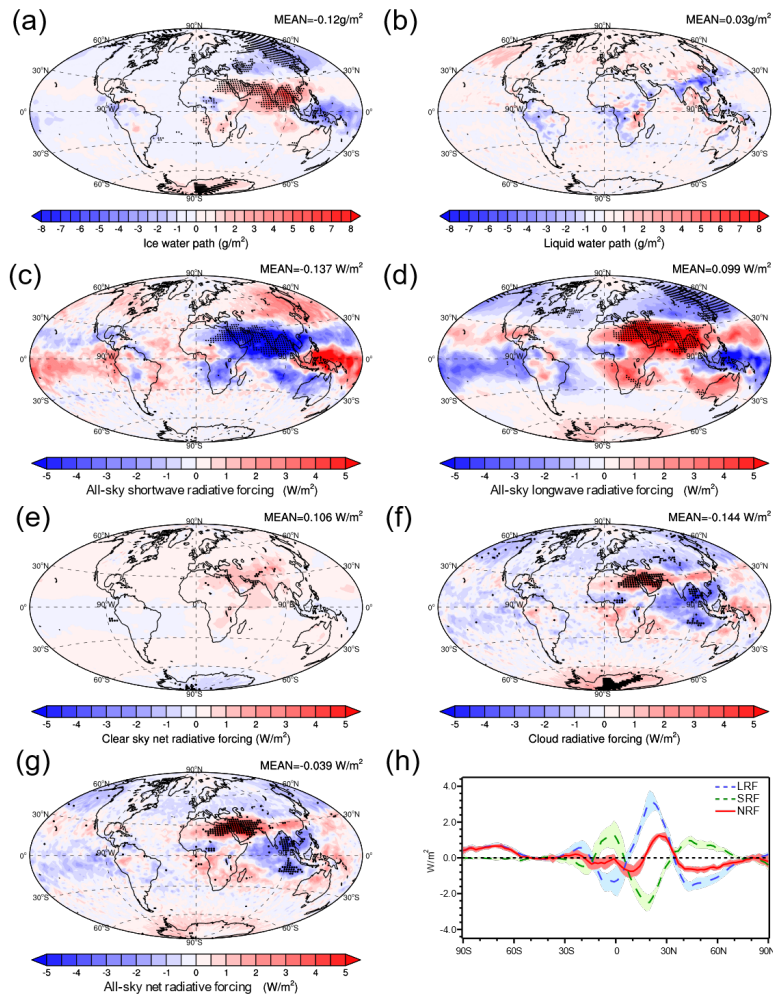
(f) Heterogeneous nucleation



1244

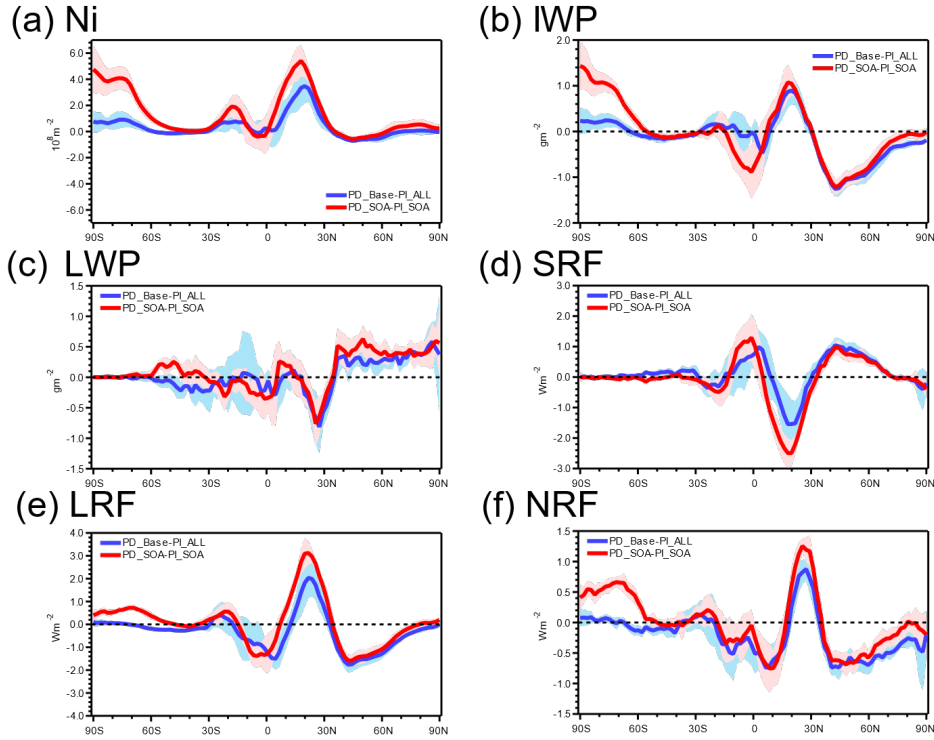
1245 Figure 11. The annual average change in column number concentration (a, c, e)
 1246 and zonal average number concentration (b, d, f) of total ice (a, b), ice from
 1247 homogeneous nucleation (c, d) and ice from heterogeneous nucleation (e, f) for the
 1248 difference between the PD_SOA and PI_SOA cases. Differences significant at the
 1249 90% level according to a Student's t test are depicted by points.

1250



1251

1252 Figure 12. Annual mean plots of the changes in ice water path (a), liquid water
 1253 path (b), all-sky shortwave radiative forcing (c), all-sky longwave radiative forcing
 1254 (d), clear sky net radiative forcing (e), cloud radiative forcing (f) and all-sky net
 1255 radiative forcing (g) as well as longwave radiative forcing (h, LRF, blue dashed
 1256 line), shortwave radiative forcing (h, SRF, green dashed line) and all-sky net
 1257 radiative forcing (h, NRF, red solid line) versus latitude for the difference between
 1258 the PD_SOA and PI_SOA cases. Differences significant at the 90% level
 1259 according to a Student's t test are depicted by points. The shading in (h) represents
 1260 one standard deviation of the interannual variation over six years.



1261

1262 Figure 13. Change in vertically integrated ice number concentration (a), ice water
 1263 path (b), liquid water path (c) as well as shortwave radiative forcing (d), longwave
 1264 radiative forcing (e) and all-sky net radiative forcing (f) for the difference between
 1265 the PD_SOA and PI_SOA cases (red line) as well as PD_Base and PI_ALL cases
 1266 (blue line). The shading represents one standard deviation of the interannual
 1267 variation over six years.

1268

1269

1270

1271

1272